Inferring the Subsurface Geometry and Strength of Slow-moving Landslides using 3D Velocity Measurements from the NASA/JPL UAVSAR

A. L. Handwerger[1,2], A. M. Booth[3], M.-H. Huang[4], and E. J. Fielding[2]

[1]Joint Institute for Regional Earth System Science and Engineering, University of California, Los Angeles, CA, USA
[2]Jet Propulsion Laboratory, California Institute of Technology, Pasadena, CA, USA
[3]Department of Geology, Portland State University, Portland, OR, USA
[4]Department of Geology, University of Maryland, College Park, MD, USA

Corresponding author: Alexander L. Handwerger (alexander.handwerger@jpl.nasa.gov)

Key Points:

- Landslide thickness can vary by tens of meters within a single landslide
- The largest landslide complexes get larger by increasing area rather than increasing thickness
- Landslide strength is scale-dependent, such that large landslides tend to be weaker than small landslides

Abstract

The hazardous impact and erosive potential of slow-moving landslides depends on landslide properties including velocity, size, and frequency of occurrence. However, constraints on size, in particular, subsurface geometry, are lacking because these types of landslides rarely fully evacuate material to create measurable hillslope scars. Here we use pixel offset tracking with data from the NASA/JPL Uninhabited Aerial Vehicle Synthetic Aperture Radar (UAVSAR) to measure the three-dimensional surface deformation of 134 slow-moving landslides in the northern California Coast Ranges. We apply volume conservation to infer the actively deforming thickness, volume, geometric scaling, and frictional strength of each landslide. These landslides move at average rates between ~0.1–3 m/yr and have areas of ~6.1 x 10^3–2.35 x 10^6 m^2, inferred mean thicknesses of ~1.1–25 m, and volumes of ~7.01 x 10^3–9.75 x 10^6 m^3. The best-fit volume-area geometric scaling exponent is $\gamma \sim 1.2–1.5$, indicating that these landslides fall between typical soil and bedrock landslide scaling. A rollover in the scaling relationship suggests that the largest landslide complexes in our dataset become large primarily by increasing in area rather than thickness. In addition, the slow-moving landslides display scale-dependent frictional strength, such that large landslide tend to be weaker than small landslides. This decrease in frictional strength with landslide size is likely because larger landslides are composed of higher proportions of weak material. Our work shows how state-of-the-art remote sensing techniques can be used to better understand landslide processes and quantify their contribution to landscape evolution and hazards to human safety.

1 Introduction

Landslides are a major natural hazard and are often the dominant process that erodes mountainous landscapes (Korup et al., 2007; Larsen et al., 2010; Mackey & Roering, 2011;

Simoni et al., 2013). Both their hazardous impact and erosive potential depend on landslide properties including the velocity, size, and frequency of occurrence. Measuring these landslide properties is challenging because landslides exhibit a wide range of velocities (mm/yr to m/s), spatial areas (10^0 - 10^8 m^2), and volumes (10^{-1} - 10^{10} m^3), and can occur in large numbers (hundreds to tens of thousands) over broad spatiotemporal scales (Cruden & Varnes, 1996; Hungr et al., 2014; Lacroix, Handwerger, et al., 2020; Larsen et al., 2010). Importantly, the landslide failure style also impacts our ability to measure landslide properties, such as thickness and volume, which can strongly influence runout and erosion rate (e.g., Korup et al., 2007; Larsen et al., 2010; Legros, 2002). Some landslides create clear and identifiable scars and deposits by evacuating material from the hillslope, making it possible to directly measure landslide properties from field data, digital elevation models (DEMs), and remote sensing observations (e.g., Bessette-Kirton et al., 2018; Warrick et al., 2019; Wartman et al., 2016). However, for landslides that move slowly for years or centuries (Lacroix, Handwerger et al., 2020; Mackey et al., 2009; Rutter & Green, 2011), referred to as slow-moving landslides, and do not create hillslope scars, it is difficult to constrain their thickness and volume because data are usually limited to isolated point measurements from boreholes (Schulz et al., 2018; Simoni et al., 2013; Travelletti & Malet, 2012), which do not capture the spatial variability exhibited by these landslides. It is therefore advantageous to develop and apply tools and methods that can be used to construct large inventories of slow-moving landslides and quantify their surface and subsurface properties.

Modern remote sensing tools, such as synthetic aperture radar (SAR), optical imagery, and lidar, provide high-resolution measurements of topography and ground surface deformation that can be used to identify and monitor landslides with millimeter- to centimeter-scale accuracy

at spatial resolutions of a few centimeters to hundreds of meters. Recent work using pixel offset tracking and SAR interferometry with these data has quantified the two-dimensional (2D) and three-dimensional (3D) surface deformation of slow-moving landslides (Aryal et al., 2015; Booth et al., 2020; Hu et al., 2020; Lacroix, Dehecq et al., 2020; Stumpf et al., 2017; Travelletti et al., 2014). These studies, along with numerous ground-based investigations (e.g., Iverson & Major, 1987; Malet et al., 2002; Schulz et al., 2017), have shown that slow-moving landslides exhibit non-uniform spatial and temporal kinematic patterns. In addition, high-resolution 3D surface deformation measurements can be used to infer the thickness and subsurface geometry of the actively moving part of the landslide. Previous studies (Aryal et al., 2015; Booth et al., 2020; Booth, Lamb, et al., 2013; Delbridge et al., 2016; Hu et al., 2020) have suggested that active landslide thickness can vary by tens of meters within a single landslide, and the slip surfaces have an irregular and bumpy morphology that differs considerably from commonly assumed, idealized geometric forms, such as semicircles, ellipsoids, and log spirals (see a detailed review paper by Michel et al., 2020). These large changes in thickness within a single landslide mass have important implications for estimating volume and sediment flux, designing field instrumentation and landslide mitigation strategies, and determining the stresses that control landslide kinematics. Although techniques that invert surface observations for subsurface characteristics are becoming more common, most studies have focused on individual landslides occurring under different and site-specific environmental conditions, making it difficult to identify more generic geometric scaling relations for slow-moving landslides.

In this study, we use data from the NASA/JPL Uninhabited Aerial Vehicle Synthetic Aperture Radar (UAVSAR) to construct an inventory of 134 active slow-moving landslides in a ~ 1621 km^2 area of the northern California Coast Ranges between 2016 and 2019 (Figure 1).

These landslides occur in the Eel River catchment, a region well known for its slow-moving landslides, and are driven by high seasonal rainfall (Bennett, Roering, et al., 2016; Booth, Roering, et al., 2013; Handwerger et al., 2013, 2015; Handwerger, Fielding, et al., 2019; Handwerger, Huang, et al., 2019; Kelsey, 1978; Mackey et al., 2009; Mackey & Roering, 2011; Roering et al., 2009, 2015; Schulz et al., 2018). The landslides are underlain by the Central Belt Franciscan mélange, a mechanically weak and pervasively sheared bedrock with an argillaceous matrix that surrounds blocks of stronger rock types, including sandstone, chert and greenstone (Jayko et al., 1989; Jennings et al., 1977; McLaughlin et al., 1982, 2000). We measure the 3D surface deformation and geometry of each landslide, and use these data in a volume conservation framework to invert for their active thickness, volume, and strength. We derive new geometric scaling relations for slow-moving landslides and make comparisons with a worldwide inventory of soil and bedrock landslides. Our work is the first to use volume conservation methods to invert for the thickness of a large inventory of landslides, and this approach could be applied to other groups of slow-moving landslides around the world. Our work also shows how state-of-the-art remote sensing techniques can be used to better understand landslide processes and quantify their contribution to landscape evolution.

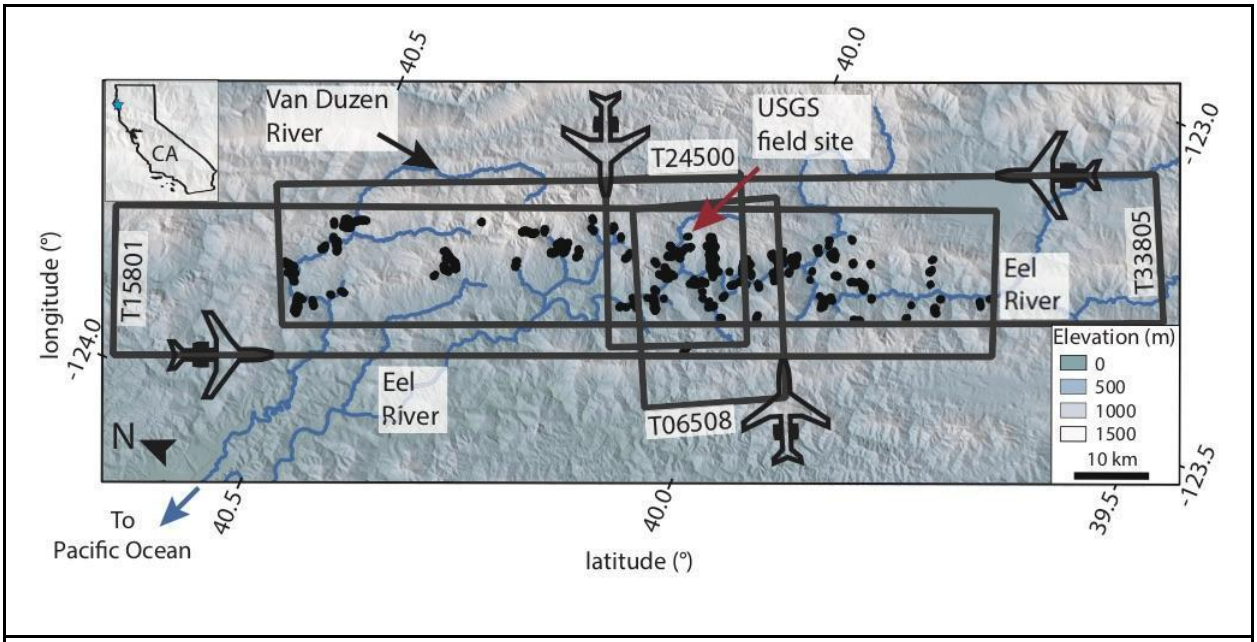

Figure 1. Map of our northern California Coast Ranges study site. Black polygons outline the active landslides analyzed in this study. Elevation (m) shown by green to white color gradient. Black boxes show the left-looking UAVSAR swaths and corresponding track numbers with airplanes showing flight direction. Red arrow shows the location of a U.S. Geological Survey (USGS) landslide field site. Blue lines show major rivers and some tributaries in landslide areas. Inset shows a map of California with a star corresponding to the study site.

2 Materials and Methods

2.1 UAVSAR Data and Processing

We use SAR data acquired by the NASA/JPL UAVSAR airborne system for our landslide investigation. UAVSAR has a left-looking radar attached to a NASA Gulfstream III airplane that operates with a L-band wavelength (~23.8 cm) and a swath width of ~20 km. The NASA Gulfstream III autopilot flies at 13 km above sea level and repeats the flight lines within a five-meter radius tube, so the spatial baselines are always short and have no impact on

126 deformation measurements. UAVSAR data have a pixel spacing of 1.67 m in the range direction
127 (measured along the line-of-sight, LOS) and 0.6 m in the azimuth direction (measured along the
128 UAVSAR flight direction). We designed the UAVSAR data collection for the northern
129 California Coast Ranges site specifically to monitor a large quantity of slow-moving landslides
130 that were initially identified by several previous studies (e.g., Bennett, Miller, et al., 2016;
131 Handwerger et al., 2015; Kelsey, 1978; Mackey & Roering, 2011; Roering et al., 2009). Some of
132 these UAVSAR data were used in a recent study by Handwerger, Fielding, et al. (2019) to
133 analyze changes in landslide activity due to extreme rainfall. We collected data on 4 partially
134 overlapping flight paths to increase data redundancy and to provide between 4 and 8 independent
135 deformation measurements (Figure 1). There were 12 data acquisitions at our field site between
136 April 2016 and May 2019. The time between data acquisitions ranges between 47 and 237 days,
137 with a mean of 104 days (Table S1). UAVSAR Single-Look Complex (SLC) data are freely
138 available at https://uavsar.jpl.nasa.gov/.

139 We perform pixel offset tracking on the coregistered UAVSAR stack SLC data using the
140 *Ampcor* module, which is part of the JPL InSAR Scientific Computing Environment (ISCE)
141 version 2 software package (Rosen et al., 2012). Pixel offset tracking (sometimes referred to as
142 subpixel correlation) uses cross-correlation between SAR amplitude images to quantify image
143 offsets (i.e., displacement) due to ground surface motion in two dimensions; 1) the range or look
144 direction, and 2) the azimuth or along-track direction (e.g., Fialko et al., 2001; Fielding et al.,
145 2020; Pathier et al., 2006). We use the terms range/look direction and azimuth/along-track
146 direction, interchangeably. Pixel tracking has a precision up to ~1/10 of the pixel size, which
147 corresponds to ~6 cm in the along-track direction and ~17 cm in the range direction for a pair of
148 UAVSAR images. Although this technique is less precise than conventional InSAR, it does not

involve phase unwrapping and thus is better suited for measuring the decimeter- to meter-scale displacements commonly displayed by many slow-moving landslides (Lacroix, Handwerger, et al., 2020). To account for the differences in the range and along-track pixel size, we use a cross-correlation window length of 128 pixels with a skip size of 32 pixels (distance between matching window calculations) in the along-track direction and a cross-correlation window width of 64 pixels with a skip size of 16 pixels in the range direction, resulting in a window size of 77 m by 107 m. This cross-correlation window size was found to provide the best landslide deformation signal from UAVSAR pixel offset tracking by Handwerger, Fielding et al. (2019). We geocode the pixel offset measurements to a 0.4 arcsecond (~12 m) pixel using the TanDEM-X DEM provided by the German Aerospace Center (DLR). We process all possible combinations of pixel offset tracking pairs, which results in 66 pixel offset tracking maps on each track (264 in total) with single pair time spans ranging from 47 to 1148 days (Table S1). We exclude 35 poor-quality pixel offset tracking maps from our analysis that included a large number of pixels with physically incorrect displacements (e.g., upslope motion or unusually large values) and significant noise that obscured the landslide signals. We found these poor-quality data tend to result from long duration pairs that exceed ~2 years, which are subject to numerous changes in the ground surface (e.g., vegetation changes, anthropogenic changes) that can deteriorate the cross-correlation result (Table S1). We convert all of the displacement offset maps to velocities and then take the temporal average of the 31 remaining pixel offset velocity maps to make a mean velocity map for our thickness inversions.

2.2 Three-dimensional Ground Surface Deformation

171 To solve for 3D deformation from SAR requires at least three independent measurements
172 of surface deformation. Each UAVSAR flight path provides two independent measurements of
173 surface motion from pixel offset tracking (i.e., along-track and range). Therefore, using pixel
174 offset tracking velocity maps, data from at least two flights is required for 3D inversions.
175 Because UAVSAR acquires data on four different flight paths in our field area (Figure 1), we
176 have a maximum of eight deformation measurements in the central region of our field area where
177 all four flight paths overlap and a maximum of two deformation measurements in the northern
178 and southern extents where only two flight paths overlap. Thus, we are always able to achieve an
179 overdetermined 3D inversion.

180 Each deformation measurement from pixel tracking is composed of the true displacement
181 vector projected onto the along-track or range direction of the UAVSAR. We use a least-squares
182 inversion to isolate the east, north, and vertical components of deformation defined in the form
183 **d** = **Gm**,

184
$$\begin{bmatrix} v_{rng1} \\ v_{azi1} \\ \vdots \\ v_{rng,M} \\ v_{azi,M} \end{bmatrix} = \begin{bmatrix} \cos\xi 1 \sin\theta_1 & \sin\xi_1 \sin\theta_1 & -\cos\theta_1 \\ \cos\xi_1 & \sin\xi_1 & 0 \\ \vdots & \vdots & \vdots \\ \cos\xi_M \sin\theta_M & \sin\xi_M \sin\theta_M & -\cos\theta_M \\ \cos\xi_M & \sin\xi_M & 0 \end{bmatrix} \begin{bmatrix} v_{ew} \\ v_{ns} \\ v_{ud} \end{bmatrix}, \quad (1)$$

185 where $v_{rng,M}$ is the range (or look direction) velocity, $v_{azi,M}$ is the azimuth (or along-track
186 direction) velocity, M is the flight path number (minimum of two needed for pixel offset
187 tracking), ξ is the UAVSAR heading direction (i.e., along track direction) with counterclockwise
188 as positive, θ is the UAVSAR look angle, and v_{ew}, v_{ns}, v_{ud} are the east-west, north-south, and
189 vertical components of velocity, respectively.

190 The overdetermination of the 3D inversion allows us to constrain the uncertainty from the
191 inversion (e.g., Delbridge et al., 2016). To constrain the inversion uncertainty, we repeat the 3D

192 inversion multiple times using different combinations of v_{rng} and v_{azi}. For instance, for landslides
193 with eight deformation measurements (i.e., four range and four azimuth measurements), we
194 perform the 3D inversion 198 times using between three and eight deformation measurements.
195 We then take the mean and standard deviation of all of the inversions and use these values as the
196 3D velocities and inversion uncertainty, respectively. We further constrain the uncertainty in our
197 velocity measurements by examining the apparent deformation rate of stable hillslopes. To
198 reduce noise and error (i.e., unrealistically large displacements), we apply velocity thresholds
199 and mask out pixels with apparent velocities > 50 m/yr, which is much faster than the typical
200 velocity range displayed by the northern California Coast Ranges landslides (Bennett, Roering,
201 et al., 2016; Handwerger, Fielding, et al., 2019; Roering et al., 2015). We also mask out pixels
202 that have mean velocities less than their inversion uncertainty and use nearest neighbor
203 interpolation with a five pixel maximum radius to fill in these masked pixels.
204
205 2.3 Landslide Thickness Inversion
206 We use 3D surface velocity measurements from pixel offset tracking to infer the
207 thickness, volume, and shear zone geometry of the active parts of each landslide using a
208 conservation of volume approach. We apply the method originally described by Booth, Lamb, et
209 al., (2013) and more recently by Booth et al. (2020), which assumes that during our ~3 year
210 study period, the measured surface velocity is representative of the depth-averaged velocity, the
211 sliding surface does not change in time, there is minimal direct erosion or deposition of the
212 landslide surface, and the landslide material density is uniform and constant. While landslides
213 may violate these assumptions in general, they are reasonable for our study area for the following
214 reasons: (1) at the Two Towers landslide, a U.S. Geological Survey (USGS) instrumented

landslide in our study site (Schulz et al., 2018), the measured surface velocity was approximately equal to the depth-averaged velocity, and a narrow shear zone was identified (Figure S1); (2) the landslides were continuously active with fixed spatial boundaries over the time periods that 3D displacements were measured, suggesting movement on the same slip surface; (3) minor amounts of direct surface erosion or deposition were likely confined to gully systems on the landslides' surfaces, which occupy a small percentage of the landslides' surface area (~1%) and therefore have a minimal effect on the inversion; and (4) dilation/compaction or shrinking/swelling that would cause changes in density is likely on the order of centimeters or less (Booth et al., 2020; Delbridge et al., 2016; Iverson, 2005; Schulz et al., 2018), which is typically small compared to surface velocity gradients, thus having limited influence of the measured 3D surface velocity. Therefore, for a landslide of constant density with no erosion or deposition, conservation of volume implies that

$$v_{ud} = \nabla \cdot (\bar{u}h) + u_{surf} \cdot \nabla z_{surf}, \qquad (2)$$

where v_{ud} is the vertical component of the 3D landslide surface velocity vector, h is the active landslide thickness, u_{surf} is the vector of horizontal components of landslide surface velocity, $\bar{u}$ is the depth-averaged vector of horizontal components of landslide velocity, and z_{surf} is the surface elevation measured from the ~12 m TanDEM-X DEM. The first term on the right-hand side of equation 2 is the contribution of flux divergence to the vertical component of the surface velocity, and the second term is the contribution due to advection of the sloped land surface. Because UAVSAR measures the velocity of the ground surface, u_{surf}, we assume that $\bar{u} = f u_{surf}$, where f is a constant that characterizes the thickness of the shear zone at the base of the landslide relative to the total landslide thickness. We constrain f using borehole inclinometer data from two boreholes at the USGS field station on the Two Towers landslide (supporting

238 information and Figure S1). Unfortunately, the Two Towers landslide is not detectable with pixel
239 tracking from UAVSAR data because the landslide is small (250 m long and 40 m wide) and
240 moving too slowly (maximum speed ~6 cm/yr) (Schulz et al., 2018). Using these data, we find
241 that $f \sim 0.96$, which indicates that the landslide moves along a narrow shear zone with the
242 material above translating essentially as a rigid block. For simplicity, we assume that $f = 1$ and
243 that the landslides move as a rigid block. Other studies in California (e.g., Keefer & Johnson,
244 1983, Swanston et al., 1995) and around the world (e.g., van Asch & van Genuchten, 1990;
245 Simoni et al., 2013) have also found that similar type slow-moving landslides move as a rigid
246 plug above a narrow shear zone such that $f \sim 1$ is a reasonable approximation, however more
247 ground-based investigations are required to better constrain the f parameter for multiple
248 landslides. Although f generically represents the ratio of depth-averaged to surface velocity, it
249 can be related to specific rheologies if desired (Booth, Lamb, et al., 2013; Delbridge et al., 2016)
250 and we discuss the implications of different f values in Section 4.2.

251 Incorporating f into equation 2 gives

252 $$v_{ud} = \nabla \cdot \left(f u_{surf} h\right) + u_{surf} \cdot \nabla z_{surf}, \qquad (3)$$

253 which is a statement of conservation of volume in a Lagrangian reference frame (Booth et al.,
254 2020; Delbridge et al., 2016). We discretize equation 3 using centered finite differences,
255 rearrange it as a system of linear equations, and then solve for thickness by minimizing the value
256 of

257 $$|Xh - b|^2 + \alpha^2 |\nabla^2 h|^2, \qquad (4)$$

258 subject to non-negative constraints,
259 where X is a diagonally dominant matrix that contains the depth-averaged horizontal velocity
260 data, b is a vector defined as $u_{surf} \cdot \nabla z_{surf} - v_{ud}$, and α is a damping parameter to regularize

the ill-posed inverse problem. Since both the matrix X and the vector b contain data with uncertainties, and the damping parameter necessarily introduces bias, estimating total uncertainty of the resulting thickness model is not straightforward. However, we make a minimum estimate following standard techniques from inverse theory, which reflects uncertainty in b only (supporting information). We explore a wide range of α from 10^{-3} to 10^{1} and determine the best level of regularization using the Generalized Cross-Validation method (supporting information and Figure S2). We resample our ~12 m pixel spacing grid to square 10 m x 10 m pixel and perform the thickness inversion in the MATLAB software package using the CVX program, a package for specifying and solving convex programs (Grant & Boyd, 2014). For the largest landslide in our inventory (i.e., Boulder Creek landslide complex) we had to downsample the grid to a 20 m x 20 m pixel due to computational limitations. The inferred thickness values represent the best solution that does not violate conservation of volume and assumes that the surface velocity is equal to the depth-averaged velocity.

It is important to further emphasize that the thickness inversions are only relevant to the active parts of landslides such that there needs to be detectable surface deformation to invert for the landslide thickness. Specifically, the values of b (equation 4) need to differ from background values on known stable ground to infer non-zero thicknesses. Landslides or areas and kinematic zones within landslides that are not moving are therefore considered to have zero depth. Landslide thickness in this study therefore specifically means the “active thickness” during our study period.

2.4 Landslide Inventory and Geometric Scaling

283 To select landslides for 3D surface velocity and thickness inversions, we assemble a new
284 inventory of active landslides in our ~1621 km^2 study area in the northern California Coast
285 Ranges that includes only those landslides that show a significant deformation signal using the
286 pixel offset tracking method. This limits our analysis to the faster-moving landslides that exhibit
287 rates of decimeters to meters per year. Our landslide inventory was guided by a number of pre-
288 existing landslide inventories for the northern California Coast Ranges (Bennett, Miller, et al.,
289 2016; Handwerger, Fielding, et al., 2019; Kelsey, 1978; Mackey & Roering, 2011). We map the
290 landslide boundaries in QGIS using the 3D velocity maps, hillshade maps constructed from 1 m
291 pixel spacing lidar provided by OpenTopography (Roering, 2012), the ~12 m pixel spacing
292 TanDEM-X DEM, and Google Earth imagery. Because slow-moving landslides display non-
293 uniform spatial kinematic zones and complex kinematic histories (e.g., Nereson & Finnegan,
294 2019; Schulz et al., 2017; Stumpf et al., 2017), there are often differences between the landslide
295 boundaries mapped with kinematic data and those mapped based on geomorphic interpretation of
296 hillshades or aerial photos. These differences in mapping are especially important for our
297 thickness inversions because including the parts of landslides that are not currently moving can
298 cause the thickness inversion to produce unreliable results. Therefore, we use the temporally
299 averaged landslide velocity and only map areas of each landslide that are moving during our
300 study period. For larger landslides with multiple kinematic zones, we perform separate thickness
301 inversions for any isolated, faster-moving areas of the landslide, as well as for the entire
302 landslide complex as a whole. If results had substantially different spatial patterns of thickness,
303 we adopt the more reliable results for the smaller isolated landslides. We use QGIS to quantify
304 the spatial metrics of each landslide, including length, average width (defined as area divided by

length), area, and slope angle. We also report the mean, median, 75th percentile, and maximum horizontal velocity, 3D velocity magnitude, and 3D inversion velocity errors for each landslide.

We then derive empirical geometric scaling relations for landslide thickness (h) and volume V from the measured landslide area A. Geometric scaling relations are commonly used to quantify erosion rates of large inventories of landslides and are important for understanding landslide mechanics (e.g., Bunn et al., 2020a; Guzzetti et al., 2009; Larsen et al., 2010; Milledge et al., 2014). Larsen et al. (2010) showed that these scaling relations hold over 9 orders of magnitude in area and 12 orders of magnitude in volume. Landslide scaling relations take the form of a power function where

$$V = c_V A^{\gamma} \text{ and } h = c_h A^{\zeta}, \qquad \text{(5a and 5b)}$$

where γ and ζ are scaling exponents and c_V and c_h are the intercepts. We constrain the coefficients of these power functions by log-transforming our data and finding the best-fit parameters with 95% confidence intervals using a linear least square inversion in MATLAB.

2.5 Frictional Strength

We estimate the frictional strength of each landslide by following the 3D Simplified Janbu method (Bunn et al., 2020b; Hungr, 1987; Hungr et al., 1989; Leshchinsky, 2019). This method assumes that the vertical intercolumn shear forces are negligible. Each landslide is discretized into 3D columns with a surface area S_{basal} and total weight W. The basal surface area is defined by

$$S_{basal} = \Delta x \Delta y \frac{(1-\sin^2 \beta_y \sin^2 \beta_x)^{1/2}}{\cos \beta_y \cos \beta_x}, \quad (6)$$

where Δx and Δy are the grid spacing in the x and y direction, respectively, β_x is the local dip angle perpendicular to the direction of motion and β_y is the local dip in the direction of motion. The normal force N at the base of each column is defined by

$$N = \frac{W - CS_{basal} \sin \beta_x / F + pS_{basal} \tan \phi \sin \beta_x / F}{\cos \Delta_z \left(1 + \frac{\sin \beta_x \tan \phi}{F \cos \Delta_z}\right)}, \quad (7)$$

where p is the mean pore pressure acting at the base of each column, C is the cohesion, ϕ is the residual friction angle, F is the factor of safety, and Δ_z is the local dip angle defined in terms of the motion-parallel and motion-perpendicular dips by

$$\cos \Delta_z = \left(\sqrt{\frac{1}{1 + \tan^2 \beta_y + + \tan^2 \beta_x}} \right). \quad (8)$$

Finally, F is defined by

$$F = \frac{\sum CS_{basal} \cos \beta_x + (N - pS_{basal}) \tan \phi \cos \beta_x}{\sum N \cos \Delta_z \tan \beta_x}, \quad (9)$$

where the summation is over all columns. The numerator is the resisting force, with the term in the parentheses defining the effective normal force, and tanϕ is the friction coefficient, and the denominator is the shear force. We assume that cohesion is negligible since these landslides are moving, some of which have been moving for decades (Mackey and Roering, 2011). We set F = 1 (i.e., balanced forces at failure) and solve for friction angle under both dry and fully saturated (hydrostatic conditions) end members to produce a minimum and maximum estimate. Table S2 shows the dry and wet landslide density values used for our calculations. Recent work by Bunn et al., (2020b) used a similar approach to infer the strength of several hundred landslides in Oregon, USA.

3 Results

3.1 Landslide Inventory and 3D Velocity

We identified 134 active landslides in our northern California Coast Ranges field site (Figure 1), 19 of which were unmapped by previous studies (Bennett, Miller, et al., 2016; Handwerger, Fielding, et al., 2019; Mackey & Roering, 2011). These landslides have average widths from 66 to 556 m, lengths from 68 to 4727 m, areas from 7.8 x 10^3 to 2.63 x 10^6 m^2, and mean slope angles from 10 to 29 degrees (Table S3). Each landslide exhibited a non-uniform spatial velocity pattern (see examples in Figure 2). The spatial kinematic patterns remain fixed during our study period and are similar to those mapped in previous studies (see Bennett, Roering, et al., 2016; Handwerger, Fielding, et al., 2019; Mackey & Roering, 2011). The maximum 3D velocity magnitude of the individual landslides, calculated as $v_{3D} = (v_{ns}^2+v_{ew}^2+v_{ud}^2)^{1/2}$, ranged from 0.198 to 8.58 m/yr. The average 3D velocity magnitude of the individual landslides ranged from 0.123 to 2.11 m/yr. The landslide motion was always primarily in the downslope direction (see example in Figures 2e and 2f), but at different locations we do measure areas of both uplift and subsidence within a single landslide (see example in Figure 2d). We note that local surface uplift occurs when the vertical component of the velocity vector dips less steeply than the topographic surface at a given point. As a result, the vertical velocity is often still negative even in areas where the topographic surface is locally being uplifted, and only when the vertical motion is upwards relative to horizontal do we observe positive vertical velocities. The mean 3D velocity uncertainty from the 3D inversion (equation 1) for the individual landslides ranged from 0.0179 to 1.91 m/yr. We report the full uncertainty statistics for each individual landslide in Table S3. The 3D velocity magnitude uncertainty from examining the apparent velocity of stable hillslopes was $\leq$ 0.1 m/yr.

We classified the slow-moving landslides into three subgroups based on their geometry and kinematic patterns (Table S3). Figure 2 shows three example landslides which we define as

371 slumps, earthflows, and landslide complexes. The landslide complex shown in Figure 2 is the
372 largest landslide in our dataset and is also known as the Boulder Creek landslide in several other
373 studies (e.g., Bennett, Miller, et al., 2016; Bennett, Roering, et al., 2016; Handwerger et al.,
374 2015, 2015; Handwerger, Fielding, et al., 2019; Handwerger, Huang, et al., 2019; Mackey &
375 Roering, 2011; Roering et al., 2009). We defined slumps as landslides with lower length/width
376 aspect ratios (median = 1.57 ± 1.00, ±1 standard deviation), a strong signal of positive vertical
377 velocity components in the toe and negative vertical velocity components in the source area, and
378 one primary kinematic zone (Figure 2a). We defined earthflows as those with medium aspect
379 ratios (median = 3.56 ± 1.88, ±1 standard deviation), one primary kinematic zone, and small
380 magnitude, but mostly negative, vertical velocity components (Figure 2b). And we defined
381 landslide complexes as those with higher aspect ratios (median = 5.13 ± 2.34, ±1 standard
382 deviation), that are composed of multiple kinematic zones or even multiple landslides that
383 coalesce into a single landslide mass (Figure 2c). Landslide complexes are relatively common in
384 areas with slow-moving landslides (e.g., Cerovski-Darriau & Roering, 2016; Keefer & Johnson,
385 1983; Simoni et al., 2013). 33% of our inventory were classified as slumps, 31% as earthflows,
386 and 36% as landslide complexes. The mean 3D velocity magnitude was 0.585, 0.606, and 0.670
387 m/yr for slumps, earthflows, and landslide complexes, respectively.
388
389

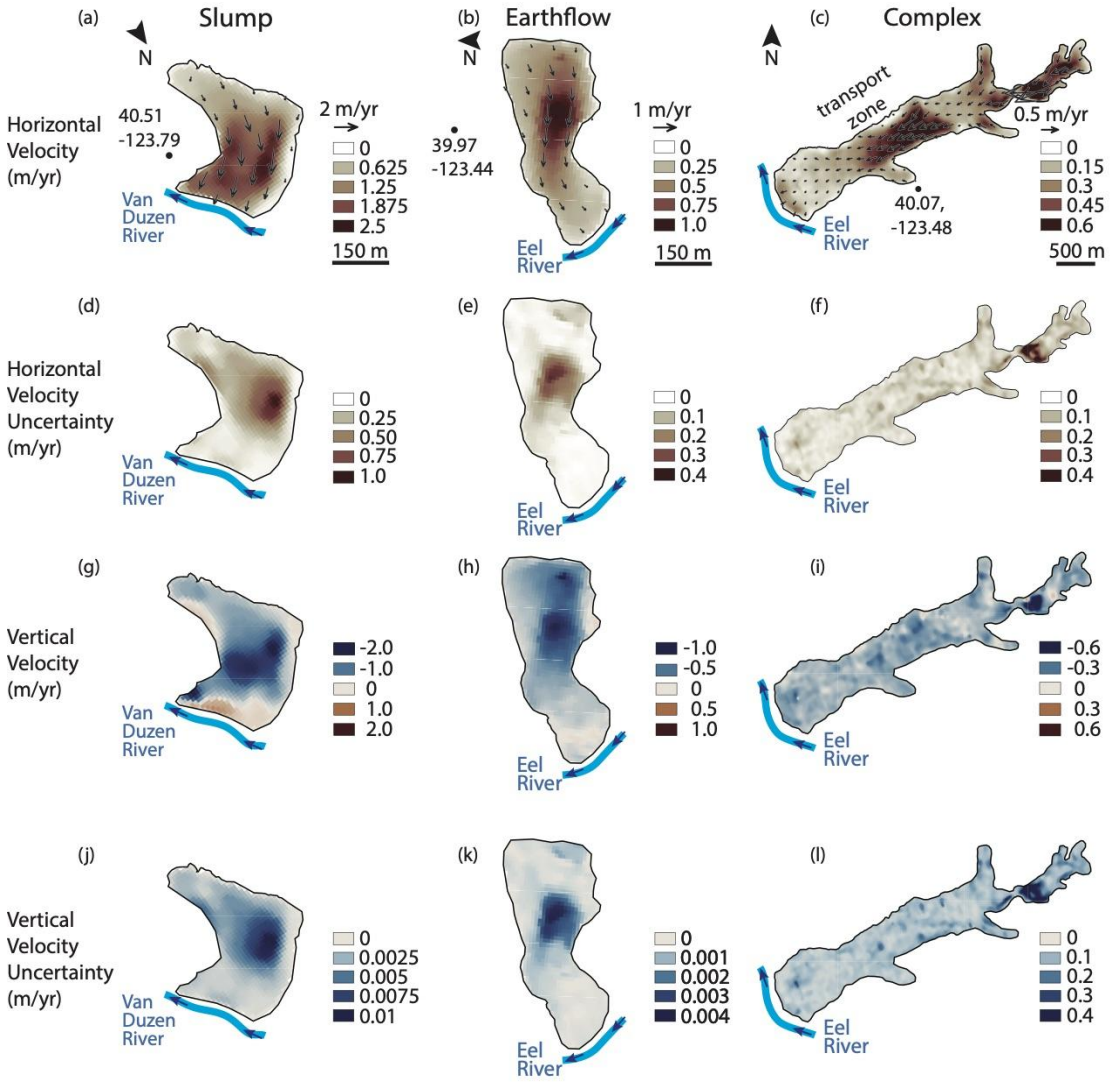

Figure 2. 3D velocity maps for example slump, earthflow, and landslide complex. (a–c) Horizontal velocity maps. Black arrows show horizontal vectors. Black circle shows latitude and longitude coordinates. (d–f) Horizontal velocity inversion uncertainty maps. (g–i) Vertical velocity maps for the three landslides. (j–l) Vertical velocity inversion uncertainty maps. Negative values correspond to vertically downward motion. Thick blue lines show the approximate location of the river channel at the toe of each landslide with dark blue arrows showing water flow direction.

3.2 Thickness, Volume, and Geometric Scaling Relations

The non-uniform kinematic patterns exhibited by these landslides are also reflected in their inferred subsurface geometry (Figure 3). We find that the thickness of each landslide varies spatially and can vary by tens of meters within the landslide boundaries. The slip surfaces are generally concave-up, but are rough and irregular in places, especially for landslide complexes. The mean active thickness of the individual landslides ranged from 0.4 to 22.4 m, and the maximum active thickness ranged from 2.25 to 89.6 m. The mean, median, minimum, maximum, and standard deviation active thickness for each landslide are reported in Table S3.

We calculated the minimum thickness uncertainty from uncertainties in the data in vector *b* following standard inverse theory for a sample of seven landslides representing the variety of style, size, and shape found in the study population (supporting information). We found that minimum thickness uncertainty increased with landslide size (Figure S3), ranging from ±1.5 to ±3.8 m from the smallest to largest landslide sampled. To reduce computation time, we estimated the minimum thickness uncertainty for each landslide using a power function (Figure S3d) and propagated these uncertainties into the landslide volume calculations (Table S3).

Next we describe our thickness inversion results for the three example types of landslides shown in Figure 2. We note again that these landslides represent their subgroups to first order. The example slump has one primary deep zone and the slip surface has a concave-up profile (Figure 3a). The slope of the slip surface deviates from the ground surface and is steeper near the headscarp and gentler near the toe. Some areas within the head of the landslide are inferred to have no active thickness because the values of *b* (equation 4) are slightly negative near the headscarp (Figure S4). For *b* to be negative, the divergence of the horizontal landslide flux (first term on the right-hand side of equation 3) must also be negative, which requires the landside

413 thickness to decrease in the direction of movement. This is not physically possible because the
414 landslide thickness is by definition zero at the headscarp, so an inferred thickness of zero
415 minimizes the misfit there.

416 The example earthflow generally has a concave-up slip surface with some irregular
417 bumps (Figure 3b). The slip surface more closely mimics the ground surface in the main
418 transport zone, however there are some low thickness zones near the headscarp and landslide
419 margins that result from negative *b* values (Figure S4). Lastly, the example landslide complex
420 (Boulder Creek landslide complex) has several different active zones, each with an alternating
421 concave-up and convex-up slip surface profile (Figure 3c). The landslide slip surface is rough
422 and irregular over the length of the entire landslide, but each deep zone generally corresponds to
423 the different kinematic units that comprise the landslide complex (Figure 2c). This large
424 landslide has several areas that do not have a resolvable active thickness. These patches with low
425 active thickness result from low velocity zones (i.e., the landslide toe) and the same
426 characteristics of the velocity field described for the example slump and earthflow (Figures S4).
427 Patches with negative *b* values must have negative flux divergence, which tends to force the
428 inferred thickness to decrease in the direction of movement at those locations.

429 Landslide zones with approximately zero inferred thickness should correspond to parts of
430 landslides that are not currently active, however, as shown in Figure 3, we also observed low
431 thickness zones in areas with detectable landslide motion. These low thickness areas in our
432 inversions are likely a consequence of issues related to our landslide mapping, noisy velocity or
433 slope data, or violations of the conservation of volume assumptions (e.g., non-uniform landslide
434 density), and are better interpreted as zones where thickness is undefined, rather than where
435 thickness is low. Because it is not possible to independently identify the exact cause of the

negative *b* values that result in low thickness zones with our dataset, we exclude these low thickness zones (< 0.1 m) from our analyses since the thickness is not determined there. We selected this threshold because it characterizes the typical thin soil depth in the Central Belt Franciscan mélange (Hahm et al., 2019). We find these areas typically correspond to regions near the landslide margins for slumps and earthflows, but are scattered throughout the body of larger landslide complexes, downflow from regions with negative *b* values (Figure 3). After excluding the low thickness zones, the mean active thickness of the individual landslides ranged from 1.06 to 25.4 m, which, as expected, is higher than the mean thickness range including the low thickness zones (0.4 to 22.4 m). For the remainder of the paper, we will report landslide metrics with these low thickness zones excluded and will report metrics including the low thickness zones in Table S3.

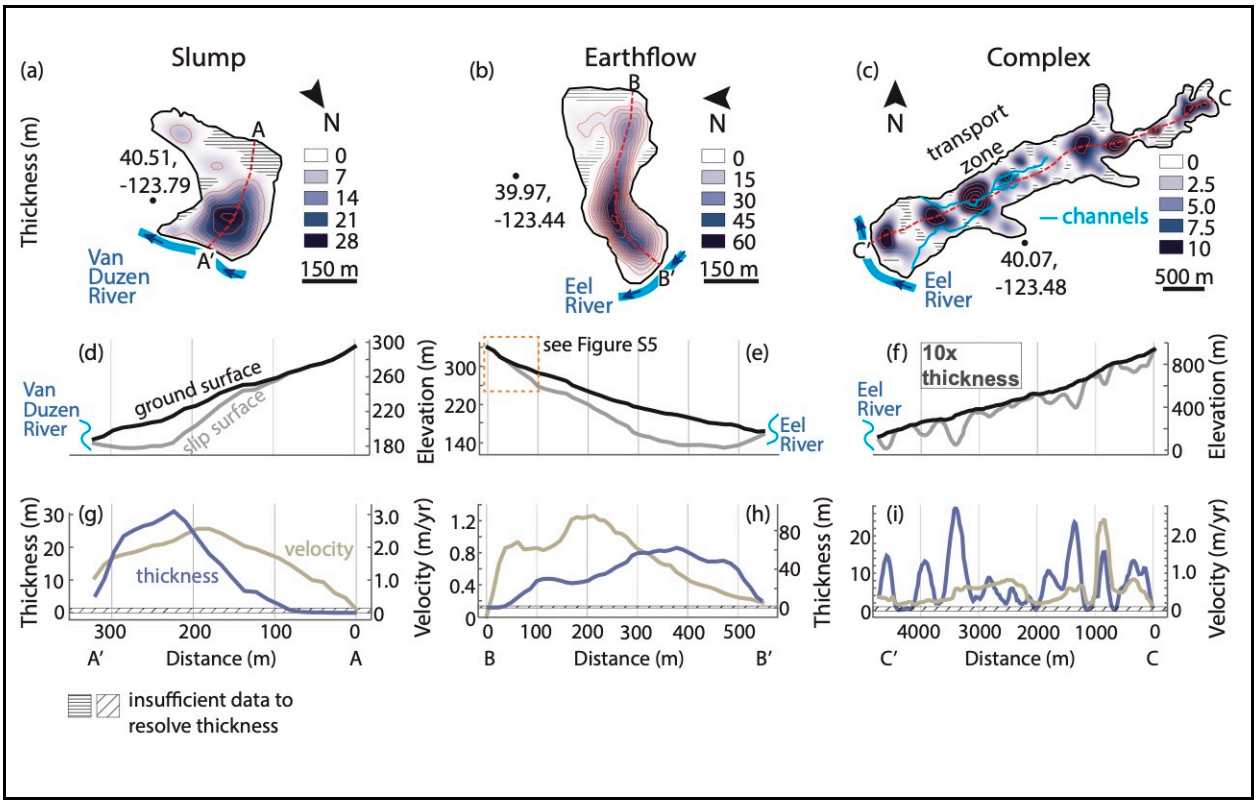

Figure 3. Landslide thickness inversions for example slump, earthflow, and landslide complex. (a–c) Landslide thickness maps. Thin orange lines show 5-meter thickness contours. Red dashed line shows profiles plotted in (d–i). Black dots show latitude and longitude coordinates. Thick blue lines show rivers and thin blue lines show deep channels incised into the landslide body. (d–f) Ground surface and slip surface elevation profiles. Dashed orange rectangle in (e) shows location of landslide headscarp in Figure S5. In subplot (f) the results of thickness inversion are vertically exaggerated by a factor of 10 relative to the elevation profile. (g–i) Landslide thickness and 3D velocity magnitude profiles. Hachures (a–c) and (g–i) identify areas with insufficient data to resolve thickness.

Although we do not have borehole data to confirm our thickness estimates, we used the topography to verify the inferred slip surface elevation in several cases. Figure S5 shows the example earthflow has a clear headscarp that can be used to trace the sliding surface underneath the ground surface. The extension of the headscarp slip surface under the landslide provides confirmation that the inversion is approximating the slip surface elevation correctly. Figure S6 shows another slow-moving landslide that has filled into a pre-existing valley. Transects across this landslide show the ground surface of the filled-in valley and that the slip surface has the shape of the pre-existing valley, providing additional confirmation that our inversions are approximating the slip surfaces correctly. In addition, we compared our thickness inversions to thickness estimates from lidar. Mackey and Roering (2011) used lidar to measure the toe height at the channel interface for dozens of landslides in the Eel River catchment, which is assumed to be minimum thickness estimates at those locations. Of those landslides, 10 (including slumps, earthflows, and complexes) can be used to make comparisons with our dataset. We found overall

good agreement between the landslides toe thickness estimated from lidar and from our inversions (Figure 4).

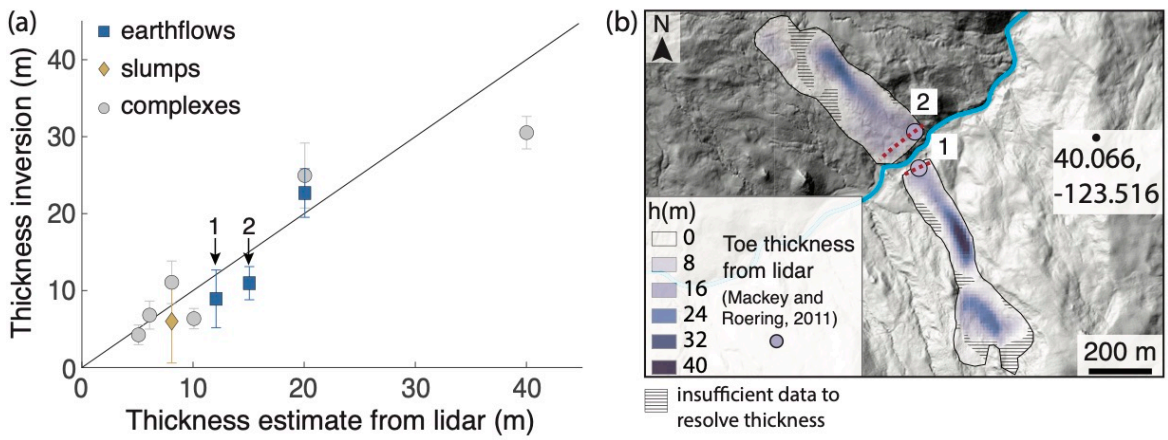

Figure 4. Landslide toe thickness estimates from lidar compared to inverted toe thickness estimates. (a) Colored symbols show inverted thickness compared to lidar estimates for 10 slumps, earthflows, and landslide complexes. We calculated the inverted toe thickness from profiles extracted across the toes and show the mean and standard deviation with error bars. Black line shows 1-to-1 line. (b) Two example landslide thickness maps draped on a lidar hillshade. Labels 1 and 2 correspond to the data points shown in (a). Hachures show zones with insufficient data to resolve thickness. Blue line shows the river channel. Red dashed line shows the profile line used to calculate toe thickness from the inversion. Toe thickness from Mackey and Roering (2011) is shown by the colored circles with black outline.

Using our thickness inversions for each landslide, we estimate that the individual landslide volumes range from 7.012 x 10^3 to 9.747 x 10^6 m^3 (Figure 5 and Table S3). Figure 5 also shows the distribution of mean thickness, area, and volume for each landslide type. Slumps are the smallest landslide type with a median thickness of 5.49 ± 2.99 m (±1 standard deviation),

468 median area of 2.71 ± 2.05 x 10^4 m^2, and median volume of 1.53 ± 1.88 x 10^5 m^3. Earthflows are
469 medium sized with an inventory median thickness of 6.99 ± 5.33 m, median area of 4.99 ± 3.26 x
470 10^4 m^2, and median volume of 2.87 ± 5.36 x 10^5 m^3. And landslide complexes are the largest
471 landslides, with a median thickness of 8.05 ± 4.34 m, median area of 1.58 ± 3.46 x 10^5 m^2, and
472 median volume of 1.22 ± 2.19 x 10^6 m^3.

473 We fit a power function to the volume-area to characterize the geometric scaling relations
474 (equation 5a) for these slow-moving landslides. We also compared our inventory to a worldwide
475 inventory of soil, undifferentiated, and bedrock landslides compiled by Larsen et al. (2010). We
476 find that the slow-moving landslides in the northern California Coast Ranges are larger in both
477 area and volume than most soil landslides, but smaller than the largest bedrock landslides around
478 the world (Figure 5). The best fit volume-area power function exponent (with 95% confidence)
479 for our inventory was γ = 1.306 (1.213, 1.399) (Figure 5). We observed an apparent break in the
480 slope of the volume-area relation for the largest landslides in our inventory with area > 10^5 m^2.
481 To further investigate this break in slope, we also fit volume-area scaling as a function of
482 landslide type and find that the break in slope is primarily associated with the landslide
483 complexes. By fitting a power function to each landslide type, we find slumps γ_S = 1.493 (1.224,
484 1.762), earthflows γ_{Ef} = 1.535 (1.273, 1.796), and complexes γ_C = 1.172 (0.9858, 1.357).
485 Although these parameters are not statistically distinct at the 95% confidence level, the fact that
486 γ_S and γ_{Ef} overlap more with each other than with γ_C supports the argument that the break in slope
487 is likely related to landslide type. We report all of the geometric scaling parameters in Table S4.

488 In addition, we calculated the thickness-area scaling relations using the mean thickness
489 (equation 5b) to represent each landslide (Figure 5). We compared these scaling relations to
490 point based estimates (lidar) and measurements (boreholes) of landslide thickness for slow-

moving landslides in the northern California Coast Ranges (Mackey and Roering, 2011) and the Reno River catchment, Apennines, Italy (Simoni et al., 2013). The best fit thickness-area power function exponent (with 95% confidence) for the inventory $\zeta = 0.3058$ (0.2129, 0.3987), indicating a weak increase in mean thickness with area for the inventory as a whole. We also fit thickness-area scaling as a function of landslide type and find slumps $\zeta_S = 0.4926$ (0.2236, 0.7615), earthflows $\zeta_{Ef} = 0.5348$ (0.2734, 0.7963), and for landslide complexes $\zeta_C = 0.1716$ (-0.0142, 0.3573). Therefore, landslide thickness significantly increases with area for slumps and earthflows (p-value = 0.0002 and 0.0006, respectively), but does not significantly vary with area for landslide complexes (p-value = 0.0694).

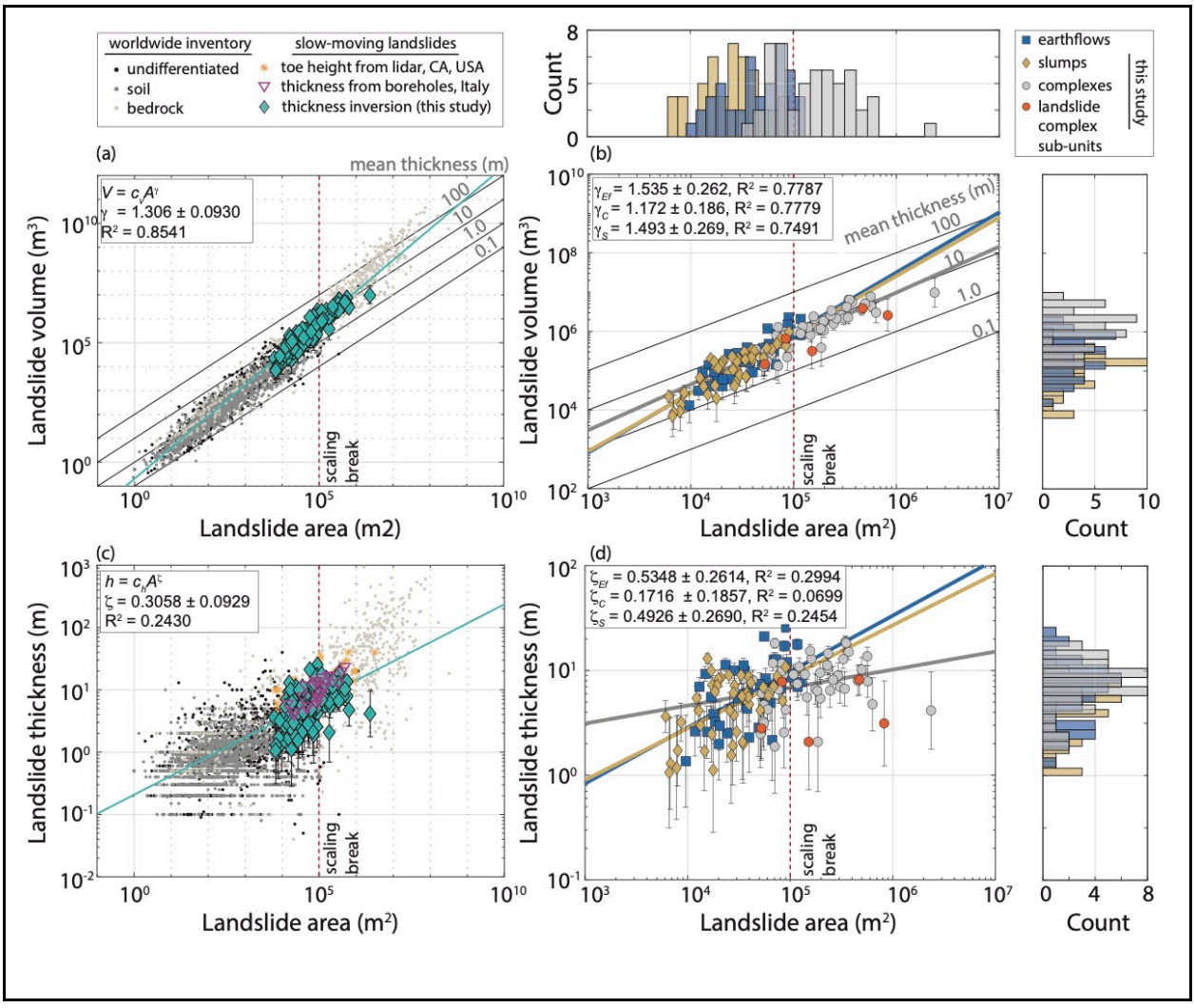

Figure 5. Landslide thickness, volume, and area geometric scaling relations. (a) Volume-area relations for our inventory and a worldwide inventory of soil, undifferentiated, and bedrock landslides (Larsen et al. 2010). (b) Volume-area relations for slumps, earthflows, and landslide complexes. (a, b) Thin diagonal black lines show volume-area for various constant mean thicknesses. (c) Thickness-area relations for our inventory (mean thickness), the worldwide inventory (Larsen et al., 2010), and slow-moving landslides in the northern California Coast Ranges (Mackey and Roering, 2011) and the Apennine mountains, Italy (Simoni et al., 2013). (d) Landslide thickness-area relations by landslide type. Orange circles in (b, d) correspond to the Boulder Creek landslide complex split into 5 smaller landslides (see Figure S7). Error bars show estimated minimum uncertainty estimates (supporting information). Red dashed vertical line shows an apparent break in scaling for the largest landslide complexes in our dataset. Histograms of landslide thickness, area, and volume show the size distributions for each landslide type. All fit parameter values are in Table S4.

3.3 Frictional Strength

Using equation 9, we back-calculated the landslide friction angle ϕ under dry and saturated conditions end members assuming nil cohesion. Additional landslide properties used in computations are listed in Table S2. The inferred friction angle ranged from ~6.8° to ~28° for dry conditions and ~13° to ~54° for saturated conditions (Table S3). Our inferred friction angles encompass friction angle values measured in the laboratory for Franciscan mélange rocks and landslide material (Figure 6). We also analyzed the friction angle as a function of landslide size and mean slope angle (Figure 6). We found a weak decreasing power-function relationship with increasing size and a linear increasing relationship with mean slope angle. The negative trend

510 with length indicates that the largest landslides are weaker, on average, than smaller landslides,
511 while the positive trend with mean slope angle indicates that landslides with gentle slopes are
512 weaker on average. Figure 6 also shows that the weakest landslides are the large landslide
513 complexes that have relatively gentle slope angles while slumps are the strongest and steepest
514 landslides in our inventory.

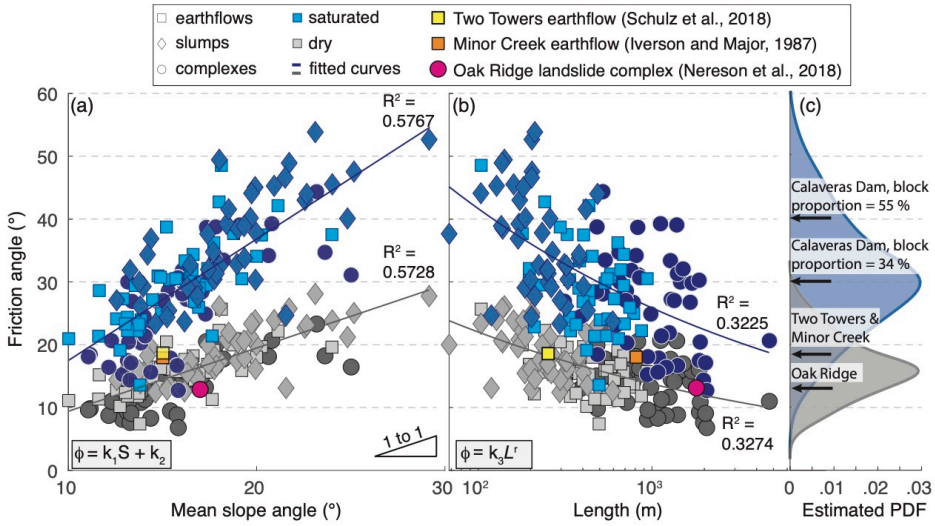

Figure 6. Inferred friction angle for dry and saturated end-members. Friction angle compared to mean hillslope angle (a) and landslide length (b). Solid line lines in (a,b) correspond to best-fit linear and power function curves. For dry conditions, best-fit parameters (with 95% confidence) k_1 = 1.009 (0.8586, 1.158), k_2 =-0.7137 (-3.279, 1.852), k_3 = 57.1 (39.66, 74.55), and r = -0.2069 (-0.2582, -0.1556). For wet conditions, k_1 = 1.935 (1.649, 2.22), k_2 = -1.816 (-6.699, 3.067), k_3 = 108.4 (74.81, 142), and r = -0.2076 (-0.2597, -0.1555). (c) Estimated probability density function for the full inventory. Black arrows and colored symbols show lab-based and back-calculated friction angle values for the Franciscan mélange hosted Oak Ridge (Nereson et al., 2018), Two Towers (Schulz et al., 2018), and Minor Creek landslides (Iverson & Major, 1987; Iverson 2000) and the Calaveras Dam, which is founded on

Franciscan mélange (Roadifer et al., 2009). The Calaveras Dam samples are plotted for two different block-in-matrix proportions, which are reported as percentages.

4 Discussion

4.1 Landslide Kinematics

Our 3D UAVSAR velocity measurements reveal 134 active slow-moving landslides in the northern California Coast Ranges moving at average rates from cm/yr to m/yr between 2016 and 2019. The 3D velocity data confirm that the motion of these landslides is generally in the downslope direction. Many of the landslides had relatively low vertical velocities compared to their horizontal velocities that are due to the gradual slope angle (inventory mean ~ 17°) exhibited by these slow-moving landslides. However, we did observe segments with vertical uplift that tended to be at the landslide toe due to the concave-up slip surface geometry, and the tendency for longitudinal shortening in the direction of motion to occur at the toe. It is possible that a component of uplift of landslide surfaces could also result from dilation or swelling (volumetric expansion), but the magnitude is small, likely on the order of a few centimeters at most (Booth et al., 2020; Delbridge et al., 2016; Iverson, 2005; Schulz et al., 2018). Including volume changes such as this in the thickness inversion may help reduce uncertainty and improve our results, especially in the zones of low thickness found in many of the landslides, but the amount of dilation or compaction occurring throughout an entire landslide and its variation is generally unknown.

Our findings agree with previous work in this region that shows that these landslides exhibit slow, spatially non-uniform downslope motion. Several of the landslides in our study area (e.g., Boulder Creek) have been moving in this manner since at least 1944 (Bennett,

Roering, et al., 2016; Mackey & Roering, 2011). Our findings also show that pixel offset tracking with very high resolution UAVSAR data is well-suited for monitoring landslides moving at rates > 10 cm/yr. Some satellites acquire very high resolution SAR with Spotlight modes, including the German TerraSAR-X and Italian COSMO-SkyMed that could provide similar measurements (e.g., Madson et al., 2019), however these data are not open-access. Lastly, we note that there are likely active landslides or landslide zones moving below the precision of our pixel offset tracking technique (< 10 cm/yr) and therefore cannot be observed with our approach. Landslides in our inventory that contain very slow-moving zones may result in unreliable thickness estimates.

4.2 Landslide Geometry

Our study is the first (to our knowledge) to apply the conservation of volume approach to invert for the thickness of multiple landslides in a given region. Previous work (Booth et al., 2020; Booth, Lamb, et al., 2013; Delbridge et al., 2016) has used the same approach to analyze individual landslides, but these landslides occur in different regions and environmental conditions. Like these previous studies, however, we found that the active landslide thickness is variable and that the slip surfaces are rough and irregular in places. The non-uniform thickness and velocity of each landslide results in a non-uniform sediment flux, which has implications for understanding sediment motion along hillslopes (Booth et al., 2020; Guerriero et al., 2017). The shape of the slip surface likely also impacts the landslide kinematics and groundwater flow (Coe et al., 2009; Guerriero et al., 2014; Iverson & Major, 1987; Keefer & Johnson, 1983). Slip surfaces that are bumpy and rough may create additional resisting stresses that act to prevent runaway acceleration and permit long periods of slow landslide motion (Baum & Johnson, 1993;

559 Booth et al., 2018; Leshchinsky, 2019). Investigation of tectonic faults and glaciers also shows
560 that slip surface roughness is an important parameter that controls frictional strength (Brodsky et
561 al., 2016; Fang & Dunham, 2013; Meyer et al., 2018).

562 For our thickness inversions we assumed that the depth-averaged velocity was equal to
563 the surface velocity (i.e., $f = 1$) for all landslides. This block on slope approximation was made
564 to simplify our regional scale analyses. Yet the borehole data from the Two Towers landslide
565 shows that $f \sim 0.96$. While changing f uniformly for each landslide does not alter the spatial
566 pattern of thickness or scaling exponents, it does impact the magnitude of the thickness and
567 therefore the volume. Setting $f = 0.96$ would cause a 4% increase in the inferred thickness and
568 volume of each landslide ($h \sim 1/f$) (Table S3). More work is needed to better constrain the depth-
569 averaged velocity for individual landslides in our field area, particularly to see if f differs with
570 landslide type. Nonetheless, our findings indicate that most of the sliding surfaces are deep-
571 seated (mean thickness for inventory ~ 7.2 m) and thus are expected to lie within the
572 unweathered Central Belt Franciscan mélange bedrock (Hahm et al., 2019). Therefore, the slow-
573 moving landslides in the northern California Coast Ranges can be classified as bedrock
574 landslides.

575 Using our landslide inventory, we developed new volume-area and thickness-area
576 geometric scaling relations for slow-moving landslides. Geometric scaling relations are
577 particularly useful for slow-moving landslides because these landslides rarely (if ever) evacuate
578 hillslopes, or create clear scars or deposits that can be easily measured. As a result, most
579 measurements of landslide thickness come from isolated boreholes, which are logistically
580 challenging and expensive to install, and are difficult to extrapolate over an entire landslide. Our
581 results provide best-fit volume-area power function exponents ($\gamma \sim 1.2 – 1.5$) that are comparable

582 to power function exponents for bedrock and soil landslides (Guzzetti et al., 2009; Larsen et al.,
583 2010; Bunn et al., 2020a). Recent work by Bunn et al. (2020a) found that deep-seated bedrock
584 landslides in Oregon, USA had $\gamma_{bedrock}$ ~1.4 – 1.6. Analysis of a worldwide landslide inventory
585 by Larsen et al (2010) showed that soil landslides had a γ_{soil} ~ 1.1 – 1.3, while bedrock landslides
586 had $\gamma_{bedrock}$ ~ 1.3 – 1.6.

587 In addition, our best-fit thickness-area scaling power exponents (ζ ~ 0. 17 – 0.53) are also
588 comparable (with a wide range) to previously published values for deep-seated landslides (Figure
589 4c). Bunn et al. (2020a) found ζ ~ 0.41 – 0.58 for deep-seated bedrock landslides. Simoni et al.
590 (2013) reported ζ = 0.44 from borehole inclinometer data from 23 slow-moving landslides in the
591 Apennine Mountains, Italy. Handwerger et al. (2013) reported ζ = 0.29 derived from lidar-based
592 estimates of landslide toe thickness from 69 landslides in the Eel River catchment, several of
593 which are also analyzed in this study (e.g., Figure 4). Importantly, neither Simoni et al. (2013) or
594 Handwerger et al. (2013) used large inventories (> 100) or spatially extensive measurements of
595 landslide thickness, which are especially important for slow-moving landslides with variable
596 thicknesses. Therefore, our new scaling relationships provide the most appropriate values for
597 deep-seated slow-moving landslides, like earthflows, and could be used to help estimate
598 sediment flux and landslide stresses in similar areas around the world. Yet, we note that the large
599 range of scaling exponents suggests that scaling relations should be used with caution. Applying
600 an incorrect scaling exponent to estimate volume for landslides with unknown thickness can lead
601 to large errors in volume calculations (Larsen et al., 2010).

602 Our findings show that the slow-moving landslides located in the northern California
603 Coast Ranges have geometric scaling exponents that lie in between the soil and bedrock type
604 landslides. However, examining the best-fit power function exponents by landslide type suggests

that slumps and earthflows display close to self-similar scaling ($\gamma_{self\text{-}similar}$=1.5), which is characteristic of bedrock landslides, while landslide complexes display scaling that is characteristic of soil landslides. Figure 5b shows that the landslide complexes with the largest areas display a scaling that tends to follow a constant mean thickness. We propose that landslide complexes have scaling relations that are close to soil landslides because: 1) the mean landslide thickness is limited by a strong layer in the mélange (and thus are similar to soil landslides that are limited by the soil thickness), or 2) that landslide complexes are an amalgamation of multiple smaller and shallower landslides. The second explanation provides a reason for why large landslide complexes tend to have multiple kinematic units (e.g., Aryal et al., 2012; Hu et al., 2020) and further emphasizes the importance of having detailed landslide maps, especially when applying geometric scaling relations (e.g., Marc and Hovius, 2015).

4.3. Thickness Inversion Challenges

The inferred thickness of many of the slow-moving landslides, in particular the landslide complexes, can be highly variable with deeper active zones and thinner or zero thickness areas that are not currently moving (Figure 3). In addition, some patches with an inferred thickness of zero occurred in areas where $b < 0$, such that a negative divergence was required to match the observations (Figure S4). These negative b values typically arose when the product of the horizontal velocity and the topographic gradient was more negative than the vertical component of the surface velocity vector (equations 3 and 4). This situation could result from artifacts in the velocity or topographic data or from actual physical processes occurring in the landslide that would tend to increase the magnitude of the horizontal velocity, increase the magnitude of the topographic gradient, or decrease the magnitude of the vertical velocity relative to their true

values, assuming conservation of volume. In particular, one plausible physical mechanism that would decrease the magnitude of v_{ud} relative to that of u_{surf} or ∇z_{surf} is dilation of landslide material as it deforms. That increase in volume would cause an additional positive vertical component to v_{ud}. Although we cannot determine whether errors in the velocity and topographic data, or actual physical mechanisms are responsible for the low inferred thickness zones, we find dilation a plausible explanation, especially near landslide headscarps, or in other zones of extension, indicating macro-scale decreases in density.

Additionally, it is important to note that the irregular thickness patterns observed in some landslides may not align with inferred thickness based on geomorphic or structural interpretations. This discrepancy is likely related to the long-lasting geomorphic imprint that slow-moving landslides have made on the landscape. Landslide surface morphology may last for decades or longer after a landslide completely stops moving (e.g., Booth et al., 2017), which can make it challenging to infer the active landslide thickness without kinematic data. Although our approach is useful for identifying the currently active portions of landslides and inferring their thickness based on volume conservation (with assumptions), it does not allow us to infer the subsurface geometry of the often larger inactive landslide body. As a result, we emphasize the need for more comparisons between ground- and remote sensing-based investigation of landslide geometry. In particular, direct comparison between numerous ground-based measurements from boreholes and structural mapping are needed to widely test the results of our remote sensing approach. Nonetheless, we find our thickness inversions are producing reasonable estimates of landslide thickness in the cases we were able to test (Figures 4, S5, and S6).

4.4 The Boulder Creek Landslide Complex

We found that the inferred active thickness for the Boulder Creek landslide complex was particularly irregular and challenging to explain based on a priori assumptions of landslide geometry. While we expect areas that are not currently active to thin, and even have zero thickness in places (e.g., parts of the landslide toe), the active transport zone on Boulder Creek also contains thin and thick patches (Figures 3c, 3f, and 3i). One possible explanation for this variability is related to patches of local density changes (e.g., dilation) that could result in negative b values. In addition to these potential artifacts, another possible cause of these low thickness zones is related to the large channel network incised into the landslide (Figure 3). In some places the channel reaches depths of 15-20 meters (Figure S8). Since the thickness is measured as the vertical distance from the ground surface to the inferred basal sliding surface, the predicted thickness is expected to be low in places surrounding the channel if the channel depth is similar to the landslide thickness. Our findings indicate that the channel has incised to depths that approach the predicted sliding surface in several places (Figure S8). However, the channel has not incised deeper than the landslide base because we find the channel is moving with similar velocity to the surrounding regions (Figure 2c).

The distinct kinematic zones within Boulder Creek landslide complex also indicate that smaller, faster, and possibly shallower features are superimposed on a larger, slower, and possibly deeper-seated failure (Figure 2c). If multiple failure planes are indeed present, that would violate the assumption of a constant f throughout the landslide and cause unreliable thickness estimates. Specifically, the surface velocity would be much greater than the depth-averaged velocity (i.e., f would be much smaller) within the superimposed landslide. This would systematically cause the inferred thickness to be too large near the headscarp of the superimposed landslide and too shallow near its toe, since the divergence of the surface velocity

674 field would be much greater than the divergence of the depth-averaged velocity field at those
675 locations. To further explore the hypothesis that the Boulder Creek landslide complex is
676 composed of multiple smaller landslides, we delineated Boulder Creek into 5 smaller sub-
677 landslides and performed a thickness inversion for each sub-landslide (Figure S7). While the
678 thickness patterns are similar to the thickness inversion for the full landslide complex, the
679 magnitude of the inferred thickness differs in some places, and the area of each landslide is
680 smaller, which places them into the space mostly populated by earthflows on the thickness-area
681 and volume-area plots (orange circles in Figures 5b and 5d). Some of these differences in the
682 magnitude of the thickness estimate are due to differences in the pixel resolution of the sub-
683 landslides (10 m pixel) and the full landslide (20 m pixel). Nonetheless, mapping landslide
684 complexes as one large landslide results in a lower mean thickness relative to the landslide area
685 which affects the geometric scaling relations. While more investigation is warranted, our
686 thickness inversions have caused us to reevaluate how we think about large landslide complexes.
687
688 4.5 Landslide Strength
689 Our back-analysis of landslide strength suggests that there is a weak decreasing
690 relationship between landslide size and strength and an increasing relationship between mean
691 slope angle and strength (Figure 6; Figure S9). The increasing relationship between mean slope
692 angle and friction angle was expected because steeper landslides must be stronger to maintain
693 force balance (equation 9). The decreasing relationship between landslide size and friction angle
694 is notable and intriguing. We hypothesize that larger landslides are weaker than smaller
695 landslides because of strength heterogeneity in the Franciscan mélange bedrock and the
696 increased likelihood of incorporating weak material within larger volumes. Laboratory

697 measurements of the strength of the Franciscan mélange rocks have shown that the proportion of
698 the blocks hosted in the argillaceous matrix controls the overall rock strength (Roadifer et al.,
699 2009) (Figure 6). This implies that larger landslides may have a decreased proportion of blocks,
700 which are not uniformly distributed, and are therefore controlled by the weak argillaceous
701 matrix.

702 Scale-dependent strength has also been observed along other landslides and faults.
703 Brodsky et al. (2016) suggested that faults are weaker at large spatial scales because they
704 encompass larger weak zones. A recent study by Bunn et al., (2020b) found that the inferred
705 shear strength of landslides decreases with increasing landslide size. They proposed that smaller
706 landslides were stronger because they occur in cemented cohesive materials and larger landslides
707 were in a residual state. Although we assumed nil cohesion to back-calculate the residual
708 frictional strength of the active landslides, it is likely that cohesion is important in controlling the
709 initial landslide failure due to the high-clay content of the Central Belt Franciscan mélange (e.g.,
710 Milledge et al., 2014).

711 Our inferred friction angles also depend on wetness conditions. Due to the high seasonal
712 rainfall in the northern California Coast Ranges, these slow-moving landslides are typically
713 saturated (or nearly saturated) during the wet season and partially saturated or dry during the dry
714 season (Hahm et al., 2019; Iverson & Major, 1987; Schulz et al., 2018). Direct comparison with
715 friction angle values measured in the laboratory and back-calculated for Franciscan mélange
716 rocks and landslide materials provides some insight into our findings. For saturated conditions
717 we find that the inferred friction angles for medium to large earthflows and landslide complexes
718 overlap the measured friction values from the Two Towers earthflow (Schulz et al., 2018), Minor
719 Creek earthflow (Iverson and Major, 1987), and Oakridge landslide complex (Nereson et al.,

2018). The majority of the smaller slumps have saturated friction angles that are significantly higher than these three landslides. The saturated friction values for smaller slumps, earthflows, and landslide complexes have more overlap with measured rock friction values that depend on the block-in-matrix proportion (Roadifer et al., 2009). Interestingly, the dry friction angles for all landslide types have more overlap with lab-based friction measurements for the landslides. Yet, it is unlikely that most of these landslides, especially the larger landslides, become completely dry. Instead, the true landslide-scale friction angle values likely lie somewhere between our inferred values for saturated and dry conditions.

We suggest that some of these differences between lab-based and inferred friction angles may be attributed to commonly observed differences in laboratory- and field-scale measurements that are often related to large scale spatial heterogeneity in the field (e.g., Marone, 1998; Van Asch et al., 2007). In addition, our assumption of nil cohesion can partially explain the higher friction values for saturated conditions (Bunn et al., 2020b). The additional strength imparted by cohesion would act to reduce the inferred friction angle values to maintain equilibrium (equation 9). We assumed nil cohesion because the landslides have moved significantly over the study period (and likely much longer), but it is likely that cohesion is important for the clay-rich landslide material and future work needs to better account for temporal changes in cohesion, which may be especially important for landslides that completely stop moving during dry periods. While the large spread of inferred friction values makes it difficult to identify a single representative value for slow-moving landslides in the northern California Coast Ranges, our results further highlight the heterogeneous nature of the Central Belt Franciscan mélange lithologic unit. Similar to the recent findings of Bunn et al., (2020b), our findings also suggest that landslide type, mean slope angle, and wetness conditions may provide some first-order

743 information on relative landslide strength at the regional scale. Furthermore, our findings have
744 implications for understanding landscape evolution and agree with previous work that shows that
745 over geomorphic timescales, we generally expect to find steeper hillslopes where hillslope
746 materials are stronger (e.g., Korup et al., 2007; Roering et al., 2015). More work is needed to
747 understand our findings in the context of landscape evolution because the currently active
748 landslides are just the most recent snapshot of the landscape, and the slopes they occur on have
749 probably been shaped by numerous previous generations of similar landslides (e.g., Mackey and
750 Roering, 2011; Roering et al., 2015).
751
752 4.6 What Controls the Size of Slow-moving Landslides?
753 Landslide size is set by the landslide mechanical properties, slope geometry, and
754 environmental conditions. For most landslides, the maximum size is typically limited to the
755 maximum hillslope size, such that the landslide length does not exceed the hillslope length. The
756 landslide thickness is typically set by the location of a weak layer beneath the ground surface, or
757 at a depth where there are changes in strength and permeability, such as the soil to bedrock
758 transition or the bottom of the critical zone (i.e., the zone that extends from the ground surface
759 down to unweathered bedrock) (Booth, Roering, et al., 2013; Larsen et al., 2010; Milledge et al.,
760 2014). Using a 3D slope stability model for shallow soil landslides that accounts for the forces
761 acting on the landslide basal slip surface, lateral margins, and passive/active wedges at the
762 toe/head, Milledge et al. (2014) found that the critical area and depth that can fail as a landslide
763 depends on the topography, pore-water pressure, and landslide material properties, including
764 density, cohesion, and friction angle. We note that their modeled landslides have less complex
765 geometries than the landslides in our inventory. In their model the pore-water pressure plays a

766 fundamental role in determining the critical landslide size and failure depth, such that higher
767 pore-water pressures decrease the critical size required for failure. Large landslides therefore
768 occur when high pore pressures are reached over a correspondingly large spatial area. At our
769 northern California Coast Range study site, the relatively thin, but laterally extensive critical
770 zone that is often saturated during the wet season (Hahm et al., 2019), may promote laterally
771 extensive landslides by elevating the water table height simultaneously over large areas.

772 Milledge et al. (2014)'s model also predicts that landslide thickness should increase as
773 the square root of the landslide area and that the failure depth sets the minimum landslide area.
774 Our best-fit thickness-area scaling exponents for slumps and earthflows are close to a square root
775 scaling (exponents ~0.5 with large 95th confidence intervals). Our results also suggest that the
776 landslide thickness controls the minimum area, but does not bound its maximum size. Instead,
777 slow-moving landslides can continue to grow in area by becoming a landslide complex
778 consisting of multiple, connected, sub-landslides without becoming significantly deeper on
779 average. Large landslide complexes can occupy multiple hillslopes, and fill valleys and
780 catchments such that their size may exceed the typical hillslope size, in contrast to landslides that
781 fully evacuate their hillslopes (e.g., Jeandet et al., 2019). Thus, it seems that the catchment size
782 sets the maximum area for slow-moving landslides. Our thickness inversion results also indicate
783 that large landslides are weaker than small landslides. This finding may indicate that large
784 landslides become large by incorporating weak material. It is possible that the largest landslides
785 grow over time and take decades to develop (e.g., Mackey & Roering, 2011). As many of our
786 landslide complexes seem to be composed of several smaller sub-landslides or kinematic zones,
787 it is possible that these features have connected through time as slip surfaces propagate along the
788 slope.

5 Conclusions

We measured the 3D surface velocity of more than one hundred slow-moving landslides in the northern California Coast Ranges with data from the NASA/JPL UAVSAR. We used volume conservation techniques to infer the active thickness, volume, and strength of each landslide. The thickness of each landslide is variable and can vary by tens of meters sometimes resulting in an irregular slip surface geometry. Volume-area geometric scaling relations suggest that these landslides have similarities to both soil and bedrock landslides around the world. Although their failure planes are likely hosted in unweathered bedrock, their thickness seems to be limited, producing a scaling similar to soil landslides for the largest landslide complexes. The inferred residual friction angles are also scale-dependent, like faults, such that large landslides complexes tend to be weaker than small landslides such as slumps. This decrease in inferred friction angle with landslide size is likely because larger landslides are composed of larger proportions of weak material. Our study represents the first to use the conservation of volume approach for numerous landslides occurring under the same environmental conditions. Our results provide key insights into the subsurface geometry and strength that control the behavior of slow-moving landslides. Our work shows how state-of-the-art remote sensing techniques can be used to better understand landslide processes for hazards and to quantify their contribution to landscape evolution.

Acknowledgements

We thank Bill Schulz for sharing data and providing a critical review of this manuscript. We thank Odin Marc, Pascal Lacroix, Amy East, and two anonymous reviewers for constructive

reviews. We thank Ben Mackey and Georgina Bennett for sharing mapped landslide polygons. Thanks to Isaac Larsen, Benedikt Bayer, and Alessandro Simoni for providing landslide size data. We thank Yang Zheng and the UAVSAR flight and data processing teams for their help with acquiring and processing the data. Part of this research was carried out at the Jet Propulsion Laboratory, California Institute of Technology, under a contract with the National Aeronautics and Space Administration (80NM0018D0004), and supported by the Earth Surface and Interior focus area.

Data Availability

Landslide geometry data used in this study are listed in the references: Larsen et al., (2010), Mackey and Roering, (2011), Simoni et al., (2013) and are included in the figures. Borehole thickness data at the Two Towers landslide is in reference: Schulz et al. (2018). Lidar digital elevation models are provided by OpenTopography and may be downloaded online (http://www.opentopography.org). OpenTopography lidar data acquisition and processing was completed by the National Center for Airborne Laser Mapping (NCALM; http://ncalm.cive.uh.edu/). NCALM funding was provided by NSF's Division of Earth Sciences, Instrumentation and Facilities Program EAR-1043051. Topographic data are also provided by the German Aerospace Center (DLR) under data proposal DEM GEOL1478 awarded to A. L. H. To acquire these data, proposals may be submitted to the DLR online (https://tandemx-science.dlr. de/). NASA/JPL UAVSAR data used in this study are freely available and may be downloaded through their website (https://uavsar.jpl.nasa.gov/).

References

Aryal, A., Brooks, B. A., Reid, M. E., Bawden, G. W., & Pawlak, G. R. (2012). Displacement fields from

point cloud data: Application of particle imaging velocimetry to landslide geodesy. *Journal of Geophysical Research: Earth Surface (2003–2012)*, *117*(F1). https://doi.org/10.1029/2011JF002161

Aryal, A., Brooks, B., & Reid, M. E. (2015). Landslide subsurface slip geometry inferred from 3D surface displacement fields. *Geophysical Research Letters*. 42(5), 1411-1417. https://doi.org/10.1002/2014GL062688

Aster, R. C., Borchers, B., & Thurber, C. H. (2013). Chapter Four - Tikhonov Regularization. In R. C. Aster, B. Borchers, & C. H. Thurber (Eds.), *Parameter Estimation and Inverse Problems (Second Edition)* (Second Edition, pp. 93–127). Boston: Academic Press. https://doi.org/10.1016/B978-0-12-385048-5.00004-5

Baum, R. L., & Johnson, A. M. (1993). Steady movement of landslides in fine-grained soils: A model for sliding over an irregular slip surface. *US Geological Survey Bulletin (USA)*.

Bennett, G. L., Roering, J. J., Mackey, B. H., Handwerger, A. L., Schmidt, D. A., & Guillod, B. P. (2016). Historic drought puts the brakes on earthflows in Northern California. *Geophysical Research Letters*, *43*(11), 5725–5731. https://doi.org/10.1002/2016GL068378

Bennett, G. L., Miller, S. R., Roering, J. J., & Schmidt, D. A. (2016). Landslides, threshold slopes, and the survival of relict terrain in the wake of the Mendocino Triple Junction. *Geology*, *44*(5), 363–366. https://doi.org/10.1130/G37530.1

Bessette-Kirton, E. K., Coe, J. A., & Zhou, W. (2018). Using stereo satellite imagery to account for ablation, entrainment, and compaction in volume calculations for rock avalanches on glaciers: Application to the 2016 Lamplugh rock avalanche in Glacier Bay National Park, Alaska. *Journal of Geophysical Research: Earth Surface*, *123*(4), 622–641. https://doi.org/10.1002/2017JF004512

Booth, A. M., Lamb, M. P., Avouac, J.-P., & Delacourt, C. (2013). Landslide velocity, thickness, and rheology from remote sensing: La Clapière landslide, France. *Geophysical Research Letters*, *40*(16), 4299–4304. https://doi.org/10.1002/grl.50828

Booth, A. M., Roering, J. J., & Rempel, A. W. (2013). Topographic signatures and a general transport law

for deep-seated landslides in a landscape evolution model. *Journal of Geophysical Research: Earth Surface*, *118*(2), 603–624. https://doi.org/10.1002/jgrf.20051

Booth, A. M., LaHusen, S. R., Duvall, A. R., & Montgomery, D. R. (2017). Holocene history of deep-seated landsliding in the North Fork Stillaguamish River valley from surface roughness analysis, radiocarbon dating, and numerical landscape evolution modeling. *Journal of Geophysical Research: Earth Surface*, *122*(2), 456–472. https://doi.org/10.1002/2016JF003934

Booth, A. M., McCarley, J., Hinkle, J., Shaw, S., Ampuero, J.-P., & Lamb, M. P. (2018). Transient Reactivation of a Deep-Seated Landslide by Undrained Loading Captured With Repeat Airborne and Terrestrial Lidar. *Geophysical Research Letters*, *45*(10), 4841–4850. https://doi.org/10.1029/2018GL077812

Booth, A. M., McCarley, J. C., & Nelson, J. (2020). Multi-year, three-dimensional landslide surface deformation from repeat lidar and response to precipitation: Mill Gulch earthflow, California. *Landslides*, 1–14. https://doi.org/10.1007/s10346-020-01364-z

Brodsky, E. E., Kirkpatrick, J. D., & Candela, T. (2016). Constraints from fault roughness on the scale-dependent strength of rocks. *Geology*, *44*(1), 19–22. https://doi.org/10.1130/G37206.1

Bunn, M., Leshchinsky, B., & Olsen, M. J. (2020a). Estimates of three-dimensional rupture surface geometry of deep-seated landslides using landslide inventories and high-resolution topographic data. *Geomorphology*, *367*, 107332. https://doi.org/10.1016/j.geomorph.2020.107332

Bunn, M., Leshchinsky, B., & Olsen, M. J. (2020b). Geologic Trends in Shear Strength Properties Inferred through Three-Dimensional Back-Analysis of Landslide Inventories. *Journal of Geophysical Research: Earth Surface*, e2019JF005461. https://doi.org/10.1029/2019JF005461

Cerovski-Darriau, C., & Roering, J. J. (2016). Influence of anthropogenic land-use change on hillslope erosion in the Waipaoa River Basin, New Zealand. *Earth Surface Processes and Landforms*, *41*(15), 2167–2176. https://doi.org/10.1002/esp.3969

Coe, J. A., McKenna, J. P., Godt, J. W., & Baum, R. L. (2009). Basal-topographic control of stationary ponds on a continuously moving landslide. *Earth Surface Processes and Landforms*, *34*(2), 264–

279. https://doi.org/10.1002/esp.1721

Cruden, D. M., & Varnes, D. J. (1996). Landslides: Investigation and Mitigation. Chapter 3-Landslide types and processes. *Transportation Research Board Special Report*, (247).

Delbridge, B. G., Bürgmann, R., Fielding, E., Hensley, S., & Schulz, W. H. (2016). Three-dimensional surface deformation derived from airborne interferometric UAVSAR: Application to the Slumgullion Landslide. *Journal of Geophysical Research: Solid Earth*, *121*(5), 3951–3977. https://doi.org/10.1002/2015JB012559

Fang, Z., & Dunham, E. M. (2013). Additional shear resistance from fault roughness and stress levels on geometrically complex faults. *Journal of Geophysical Research: Solid Earth*, *118*(7), 3642–3654. https://doi.org/10.1002/jgrb.50262

Fialko, Y., Simons, M., & Agnew, D. (2001). The complete (3-D) surface displacement field in the epicentral area of the 1999 Mw7. 1 Hector Mine earthquake, California, from space geodetic observations. *Geophysical Research Letters*, *28*(16), 3063–3066. https://doi.org/10.1029/2001GL013174

Fielding, E. J., Liu, Z., Stephenson, O. L., Zhong, M., Liang, C., Moore, A., et al. (2020). Surface Deformation Related to the 2019 M w 7.1 and 6.4 Ridgecrest Earthquakes in California from GPS, SAR Interferometry, and SAR Pixel Offsets. *Seismological Research Letters*. https://doi.org/10.1785/0220190302

Grant, M., & Boyd, S. (2014). *CVX: Matlab Software for Disciplined Convex Programming, version 2.1*. Retrieved from http://cvxr.com/cvx

Guerriero, L., Coe, J. A., Revellino, P., Grelle, G., Pinto, F., & Guadagno, F. M. (2014). Influence of slip-surface geometry on earth-flow deformation, Montaguto earth flow, southern Italy. *Geomorphology*, *219*(0), 285 – 305. http://dx.doi.org/10.1016/j.geomorph.2014.04.039

Guerriero, L., Bertello, L., Cardozo, N., Berti, M., Grelle, G., & Revellino, P. (2017). Unsteady sediment discharge in earth flows: A case study from the Mount Pizzuto earth flow, southern Italy. *Geomorphology*, *295*, 260–284. https://doi.org/10.1016/j.geomorph.2017.07.011

914 Guzzetti, F., Ardizzone, F., Cardinali, M., Rossi, M., & Valigi, D. (2009). Landslide volumes and
915 landslide mobilization rates in Umbria, central Italy. *Earth and Planetary Science Letters*, *279*(3–
916 4), 222–229. https://doi.org/10.1016/j.epsl.2009.01.005
917 Hahm, W. J., Rempe, D. M., Dralle, D. N., Dawson, T. E., Lovill, S. M., Bryk, A. B., et al. (2019).
918 Lithologically controlled subsurface critical zone thickness and water storage capacity determine
919 regional plant community composition. *Water Resources Research*, *55*(4), 3028–3055.
920 https://doi.org/10.1029/2018WR023760
921 Handwerger, A. L., Roering, J. J., & Schmidt, D. A. (2013). Controls on the seasonal deformation of
922 slow-moving landslides. *Earth and Planetary Science Letters*, *377*, 239–247.
923 https://doi.org/10.1016/j.epsl.2013.06.047
924 Handwerger, A. L., Roering, J. J., Schmidt, D. A., & Rempel, A. W. (2015). Kinematics of earthflows in
925 the Northern California Coast Ranges using satellite interferometry. *Geomorphology*, *246*, 321–
926 333. https://doi.org/10.1016/j.geomorph.2015.06.003
927 Handwerger, A. L., Huang, M.-H., Fielding, E. J., Booth, A. M., & Bürgmann, R. (2019). A shift from
928 drought to extreme rainfall drives a stable landslide to catastrophic failure. *Scientific Reports*,
929 *9*(1), 1569. https://doi.org/10.1038/s41598-018-38300-0
930 Handwerger, A. L., Fielding, E. J., Huang, M.-H., Bennett, G. L., Liang, C., & Schulz, W. H. (2019).
931 Widespread initiation, reactivation, and acceleration of landslides in the northern California Coast
932 Ranges due to extreme rainfall. *Journal of Geophysical Research: Earth Surface*, *124*(7), 1782–
933 1797. https://doi.org/10.1029/2019JF005035
934 Hu, X., Bürgmann, R., Schulz, W. H., & Fielding, E. J. (2020). Four-dimensional surface motions of the
935 Slumgullion landslide and quantification of hydrometeorological forcing. *Nature*
936 *Communications*, *11*(1), 1–9. https://doi.org/10.1038/s41467-020-16617-7
937 Hungr, O. (1987). An extension of Bishop's simplified method of slope stability analysis to three
938 dimensions. *Geotechnique*, *37*(1), 113–117. https://doi.org/10.1680/geot.1987.37.1.113
939 Hungr, O., Salgado, F., & Byrne, P. (1989). Evaluation of a three-dimensional method of slope stability

940 analysis. *Canadian Geotechnical Journal*, *26*(4), 679–686. https://doi.org/10.1139/t89-079
941 Hungr, O, Leroueil, S., & Picarelli, L. (2014). The Varnes classification of landslide types, an update.
942 *Landslides*, *11*(2), 167–194. https://doi.org/10.1007/s10346-013-0436-y
943 Intrieri, E., Raspini, F., Fumagalli, A., Lu, P., Del Conte, S., Farina, P., et al. (2017). The Maoxian
944 landslide as seen from space: detecting precursors of failure with Sentinel-1 data. *Landslides*, 1–
945 11. https://doi.org/10.1007/s10346-017-0915-7
946 Iverson, R. M. (2000). Landslide triggering by rain infiltration. *Water Resources Research*, *36*(7), 1897–
947 1910. https://doi.org/10.1029/2000WR900090
948 Iverson, R. M. (2005). Regulation of landslide motion by dilatancy and pore pressure feedback. *Journal*
949 *of Geophysical Research: Earth Surface*, *110*(F2). https://doi.org/10.1029/2004JF000268
950 Iverson, R. M., & Major, J. J. (1987). Rainfall, ground-water flow, and seasonal movement at Minor
951 Creek landslide, northwestern California: Physical interpretation of empirical relations.
952 *Geological Society of America Bulletin*, *99*(4), 579–594. https://doi.org/10.1130/0016-
953 7606(1987)99<579:RGFASM>2.0.CO;2
954 Jayko, A., Blake, M., McLaughlin, R., Ohlin, H., Ellen, S., & Kelsey, H. (1989). Reconnaissance
955 Geologic Map of the Covelo 30-by 60-Minute Quadrangle. *Northern California: US Geological*
956 *Survey Miscellaneous Field Investigation Map MF-2001, Scale*, *1*(100), 000.
957 https://doi.org/10.3133/mf2001
958 Jeandet, L., Steer, P., Lague, D., & Davy, P. (2019). Coulomb mechanics and relief constraints explain
959 landslide size distribution. *Geophysical Research Letters*, 46, 4258–4266.
960 https://doi.org/10.1029/2019GL082351
961 Jennings, C. W., Strand, R. G., & Rogers, T. H. (1977). Geologic map of California: California Division
962 of Mines and Geology, scale 1:750,000.
963 Jung, J., & Yun, S.-H. (2020). Evaluation of Coherent and Incoherent Landslide Detection Methods
964 Based on Synthetic Aperture Radar for Rapid Response: A Case Study for the 2018 Hokkaido
965 Landslides. *Remote Sensing*, *12*(2), 265. https://doi.org/10.3390/rs12020265

966 Kasper, van W., John A, S., William, N., & Luis, T. (2002). Data and model uncertainty estimation for
967 linear inversion. *Geophysical Journal International*, *149*(3), 625–632.
968 https://doi.org/10.1046/j.1365-246X.2002.01660.x
969 Keefer, D. K., & Johnson, A. M. (1983). Earth flows: Morphology, mobilization, and movement.
970 Washington: United States Government Printing Office. No 1264. https://doi.org/10.3133/pp1264
971 Kelsey, H. M. (1978). Earthflows in Franciscan mélange, Van Duzen River basin, California. *Geology*,
972 *6*(6), 361–364. https://doi.org/10.1130/0091-7613(1978)6<361:EIFMVD>2.0.CO;2
973 Korup, O., Clague, J. J., Hermanns, R. L., Hewitt, K., Strom, A. L., & Weidinger, J. T. (2007). Giant
974 landslides, topography, and erosion. *Earth and Planetary Science Letters*, *261*(3–4), 578–589.
975 https://doi.org/10.1016/j.epsl.2007.07.025
976 Lacroix, P., Dehecq, A., & Taipe, E. (2020). Irrigation-triggered landslides in a Peruvian desert caused by
977 modern intensive farming. *Nature Geoscience*, *13*(1), 56–60. https://doi.org/10.1038/s41561-019-
978 0500-x
979 Lacroix, P., Handwerger, A. L., & Bièvre, G. (2020). Life and death of slow-moving landslides. *Nature*
980 *Reviews Earth & Environment*, 1–16. https://doi.org/10.1038/s43017-020-0072-8
981 Larsen, I. J., Montgomery, D. R., & Korup, O. (2010). Landslide erosion controlled by hillslope material.
982 *Nature Geoscience*, *3*(4), 247–251. https://doi.org/10.1038/ngeo776
983 Legros, F. (2002). The mobility of long-runout landslides. *Engineering Geology*, *63*(3–4), 301–331.
984 https://doi.org/10.1016/S0013-7952(01)00090-4
985 Leshchinsky, B. (2019). Quantifying the influence of failure surface asperities on the basal shear
986 resistance of translational landslides. *Landslides*, *16*(7), 1375–1383.
987 https://doi.org/10.1007/s10346-019-01185-9
988 Mackey, B. H., & Roering, J. J. (2011). Sediment yield, spatial characteristics, and the long-term
989 evolution of active earthflows determined from airborne LiDAR and historical aerial
990 photographs, Eel River, California. *Geological Society of America Bulletin*, *123*(7–8), 1560–
991 1576. https://doi.org/10.1130/B30306.1

Mackey, B. H., Roering, J. J., & McKean, J. (2009). Long-term kinematics and sediment flux of an active earthflow, Eel River, California. *Geology*, *37*(9), 803–806. https://doi.org/10.1130/G30136A.1

Madson, A., Fielding, E., Sheng, Y., & Cavanaugh, K. (2019). High-resolution spaceborne, airborne and in situ landslide kinematic measurements of the slumgullion landslide in Southwest Colorado. *Remote Sensing*, *11*(3), 265. https://doi.org/10.3390/rs11030265

Malet, J.-P., Maquaire, O., & Calais, E. (2002). The use of Global Positioning System techniques for the continuous monitoring of landslides: application to the Super-Sauze earthflow (Alpes-de-Haute-Provence, France). *Geomorphology*, *43*(1–2), 33–54. https://doi.org/10.1016/S0169-555X(01)00098-8

Marone, C. (1998). Laboratory-derived friction laws and their application to seismic faulting. *Annual Review of Earth and Planetary Sciences*, *26*(1), 643–696. https://doi.org/10.1146/annurev.earth.26.1.643

Marc, O., & Hovius, N. (2015). Amalgamation in landslide maps: effects and automatic detection. *Natural Hazards & Earth System Sciences*, 15, 723–733. https://doi.org/10.5194/nhess-15-723-2015

McLaughlin, R. J., Kling, S. A., Poore, R. Z., McDougall, K., & Beutner, E. C. (1982). Post–middle Miocene accretion of Franciscan rocks, northwestern California. *Geological Society of America Bulletin*, *93*(7), 595–605. https://doi.org/10.1130/0016-7606(1982)93<595:PMAOFR>2.0.CO;2

McLaughlin, R. J., Blake, S., Jayko, M., Irwin, A., Aalto, W., Carver, K., et al. (2000). Geologic map of the Cape Mendocino, Eureka, Garberville, and southwestern part of the Hayfork 30 X 60 Quadrangles and Adjacent Offshore Area, Northern California.

Meyer, C. R., Downey, A. S., & Rempel, A. W. (2018). Freeze-on limits bed strength beneath sliding glaciers. *Nature Communications*, *9*(1), 1–6. https://doi.org/10.1038/s41467-018-05716-1

Michel, J., Dario, C., Marc-Henri, D., Thierry, O., Marina, P. I., & Bejamin, R. (2020). A review of methods used to estimate initial landslide failure surface depths and volumes. *Engineering Geology*, *267*, 105478. https://doi.org/10.1016/j.enggeo.2020.105478

1018 Milledge, D. G., Bellugi, D., McKean, J. A., Densmore, A. L., & Dietrich, W. E. (2014). A
1019 multidimensional stability model for predicting shallow landslide size and shape across
1020 landscapes. *Journal of Geophysical Research: Earth Surface*, *119*(11), 2481–2504.
1021 https://doi.org/10.1002/2014JF003135
1022 Nereson, A. L., Davila Olivera, S., & Finnegan, N. J. (2018). Field and Remote-Sensing Evidence for
1023 Hydro-mechanical Isolation of a Long-Lived Earthflow in Central California. *Geophysical*
1024 *Research Letters*, *45*(18), 9672–9680. https://doi.org/10.1029/2018GL079430
1025 Nereson, A. L., & Finnegan, N. J. (2019). Drivers of earthflow motion revealed by an 80 yr record of
1026 displacement from Oak Ridge earthflow, Diablo Range, California, USA. *Geological Society of*
1027 *America Bulletin*. 131(3-4), 389-402. https://doi.org/10.1130/B32020.1
1028 Pathier, E., Fielding, E. J., Wright, T. J., Walker, R., Parsons, B. E., & Hensley, S. (2006). Displacement
1029 field and slip distribution of the 2005 Kashmir earthquake from SAR imagery. *Geophysical*
1030 *Research Letters*, *33*(20). https://doi.org/10.1029/2006GL027193
1031 Roadifer, J. W., Forrest, M. P., & Lindquist, E. S. (2009). Evaluation of shear strength of mélange
1032 foundation at Calaveras Dam. Proceedings of U. S. Society for Dams, Annual Meeting and
1033 Conference, 29th, on "Managing Our Water Retention Systems, ", 507–521.
1034 Roering, J.J (2012). Eel River, CA: Landsliding and the Evolution of Mountainous Landscapes in
1035 collaboration with National Center for Airborne Laser Mapping (NCALM), distributed by
1036 OpenTopography. https://doi.org/10.5069/G9XS5S9P
1037 Roering, J. J., Stimely, L. L., Mackey, B. H., & Schmidt, D. A. (2009). Using DInSAR, airborne LiDAR,
1038 and archival air photos to quantify landsliding and sediment transport. *Geophysical Research*
1039 *Letters*, *36*(19). https://doi.org/10.1029/2009GL040374
1040 Roering, J. J., Mackey, B. H., Handwerger, A. L., Booth, A. M., Schmidt, D. A., Bennett, G. L., &
1041 Cerovski-Darriau, C. (2015). Beyond the angle of repose: A review and synthesis of landslide
1042 processes in response to rapid uplift, Eel River, Northern California. *Geomorphology*, *236*, 109–
1043 131. https://doi.org/10.1016/j.geomorph.2015.02.013

1044 Rosen, P. A., Gurrola, E., Sacco, G. F., & Zebker, H. (2012). The InSAR scientific computing
1045 environment. In *Synthetic Aperture Radar, 2012. EUSAR. 9th European Conference on* (pp. 730–
1046 733). VDE.
1047 Rutter, E., & Green, S. (2011). Quantifying creep behaviour of clay-bearing rocks below the critical stress
1048 state for rapid failure: Mam Tor landslide, Derbyshire, England. *Journal of the Geological*
1049 *Society*, *168*(2), 359–372. https://doi.org/10.1144/0016-76492010-133
1050 Schulz, W. H., Coe, J. A., Ricci, P. P., Smoczyk, G. M., Shurtleff, B. L., & Panosky, J. (2017). Landslide
1051 kinematics and their potential controls from hourly to decadal timescales: Insights from
1052 integrating ground-based InSAR measurements with structural maps and long-term monitoring
1053 data. *Geomorphology*, *285*, 121–136. https://doi.org/10.1016/j.geomorph.2017.02.011
1054 Schulz, W. H., Smith, J. B., Wang, G., Jiang, Y., & Roering, J. J. (2018). Clayey landslide initiation and
1055 acceleration strongly modulated by soil swelling. *Geophysical Research Letters*, *45*(4), 1888–
1056 1896. https://doi.org/10.1002/2017GL076807
1057 Simoni, A., Ponza, A., Picotti, V., Berti, M., & Dinelli, E. (2013). Earthflow sediment production and
1058 Holocene sediment record in a large Apennine catchment. *Geomorphology*, *188*, 42–53.
1059 https://doi.org/10.1016/j.geomorph.2012.12.006
1060 Stumpf, A., Malet, J.-P., & Delacourt, C. (2017). Correlation of satellite image time-series for the
1061 detection and monitoring of slow-moving landslides. *Remote Sensing of Environment*, *189*, 40–
1062 55. https://doi.org/10.1016/j.rse.2016.11.007
1063 Swanston D. N., R. R. Ziemer, & R. J. Janda (1995), Rate and mechanisms of progressive hillslope
1064 failure in the Redwood Creek basin, northwestern California, in Geomorphic Processes and
1065 Aquatic Habitat in the Redwood Creek Basin, Northwestern California, edited by K. M. Nolan,
1066 H. M. Kelsey, and D. C. Marron, U.S. Geological Survey Professional Paper 1454, pp. E1–E16,
1067 United States Government Printing Office, Washington, D.C.
1068 Travelletti, J, & Malet, J.-P. (2012). Characterization of the 3D geometry of flow-like landslides: A
1069 methodology based on the integration of heterogeneous multi-source data. *Engineering Geology*,

128, 30–48. https://doi.org/10.1016/j.enggeo.2011.05.003

Travelletti, J., Malet, J.-P., & Delacourt, C. (2014). Image-based correlation of Laser Scanning point cloud time series for landslide monitoring. *International Journal of Applied Earth Observation and Geoinformation*, *32*, 1–18. https://doi.org/10.1016/j.jag.2014.03.022

Van Asch, T. J., & Van Genuchten, P. M. B. (1990). A comparison between theoretical and measured creep profiles of landslides. *Geomorphology*, 3(1), 45-55. https://doi.org/10.1016/0169-555X(90)90031-K

Van Asch, T. W., Van Beek, L., & Bogaard, T. (2007). Problems in predicting the mobility of slow-moving landslides. *Engineering Geology*, *91*(1), 46–55. https://doi.org/10.1016/j.enggeo.2006.12.012

Warrick, J. A., Ritchie, A. C., Schmidt, K. M., Reid, M. E., & Logan, J. (2019). Characterizing the catastrophic 2017 Mud Creek landslide, California, using repeat structure-from-motion (SfM) photogrammetry. *Landslides*, 1–19. https://doi.org/10.1007/s10346-019-01160-4

Wartman, J., Montgomery, D. R., Anderson, S. A., Keaton, J. R., Benoît, J., dela Chapelle, J., & Gilbert, R. (2016). The 22 March 2014 Oso landslide, Washington, USA. *Geomorphology*, *253*, 275–288. https://doi.org/10.1016/j.geomorph.2015.10.022